NAL TR-1180T

ISSN 0389-4010
UDC 533.69.04
533.694.2

TECHNICAL REPORT OF NATIONAL AEROSPACE LABORATORY

TR-1180T

Experimental Studies of Vortex Flaps and Vortex Plates

Part.2 1.15m Span 60° Delta Wing

Kenichi Rinoie, John L. Stollery

October 1992

NATIONAL AEROSPACE LABORATORY

CHOFU, TOKYO, JAPAN

既 刊 報 告

TR-1170	高速機械式翼列曲げ振動加振装置とその特性 Development of a High-Speed Mechanical Drive System for Oscillating an Annular Blade Row in the Bending Mode	1992年7月	生沼　秀司，小林　　紘
TR-1171	ケーブル支持動的風洞試験によるNALスペースプレーンの空力モデル同定 Identifying the NAL Spaceplane Aerodynamic Model using Dynamic Wind Tunnel Tests	1992年7月	動的風洞試験グループ
TR-1172	翼型周りの流れとその計算法に関して，逆問題の解から得られる空気力学的な知見 New Aerodynamic Information Obtained from the Solution of the Inverse Problem for Aerofoils	1992年7月	重見　　仁
TR-1173	指定された状態推定精度実現のためのセンサ要求精度の導出 Calculation of the Required Sensor Accuracy to Obtain a Specified State Estimation Accuracy	1992年7月	佐々　修一，永安　正彦
TR-1174T	Numerical Calculation of Scramjet Inlet Flow	July 1992	Tomiko ISHIGURO Satoru OGAWA Yasuhiro WADA
TR-1175	MLS等航法系飛行実験 －平成2年度の実験概要－ Flight Evaluations of Approach/Landing Navigation Sensor Systems －Summary of 1990 Flight Experiments－	1992年7月	航法系飛行実験実行委員会
TR-1176T	AN EXPERIMENTAL STUDY OF TETHER REEL SYSTEM －A LABORATORY MODEL－	August 1992	YOSHIMURA Shoichi OKAMOTO Osamu
TR-1177	水素を促焼した液体酸素－ケロシンロケットの燃焼特性 Effects of Hydrogen Addition on Combustion Performance of a LOX/Kerosene Rocket	1992年9月	小野　文衛，田村　　洋 熊川　彰長，坂本　　博 佐藤　和雄，佐々木正樹 八柳　信之
TR-1178T	Some Flow Properties of Telescope Enclosures Estimated from Water Channel Tests －Application of The Flow Visualization Techniques－	September 1992	S. Shindo, K. Sakata, H. Ando, L. Barr, A. Miyashita
TR-1179	超音速デルタ翼の振動特性と安定限界の推定 第2報　非定常な不規則応答の局所定常時系列解析 Estimation of Critical Values and Vibration Characteristics on Supersonic Delta Wings Part 2 Locally-Stationary Time Series Analysis of Nonstationary Random Responses	1992年9月	峯岸　正勝，安藤　泰勝 松崎　雄嗣，江尻　　宏 榊原　盛三，野田　順一 石田　清道，関根　英夫 楯　　篤志，渡辺　光則

Experimental Studies of Vortex Flaps and Vortex Plates Part 2 1.15 m Span 60° Delta Wing

Kenichi RINOIE [*1] and John L. STOLLERY [*2]

ABSTRACT

Low-speed wind tunnel tests were carried out on several vortex flap and vortex plate configurations to assess their benefits. The force and surface pressure measurements were taken using a 1.15 m span, 60° delta wing model. Results indicate that the vortex flap deflection angle, which causes the flow to come almost smoothly onto the flap surface without any large separation, shows a much higher lift/drag ratio than the flap deflection angle which forms a leading-edge separation vortex over the flap surface. It was also found that there is no benefit in vortex flap deployment at incidences higher than the stall incidence. The performance of a vortex plate protruding from the leading-edge of the datum delta wing is shown to be comparable to that of the vortex flap. However, when the vortex plate is used with the vortex flap deflected, these tests showed no benefits.

Keywords: low-speed aerodynamics, delta wing, vortex flap, leading-edge separation vortex

概　　要

デルタ翼の低速空力特性を改良することを目的として，ボルテックス・フラップとボルテックス・プレート付きのデルタ翼について，その空力特性を計測した。この第2報では，スパン長1.15m，後退角60°のデルタ翼模型を用いて模型に働く空気力と表面圧力分布を測定した。その結果，模型下方へ折り曲げたボルテックス・フラップの表面に大きな前縁剥離渦が形成されない特定の迎角の場合では，前縁剥離渦がフラップ上に形成される場合よりも，デルタ翼の揚抗比が大きな値を示すことが確められた。失速角より大きな迎角ではボルテックス・フラップの効果が無いことが示された。またボルテックス・プレート（デルタ翼下面前縁に取り付けた一種のスプリットフラップ）を用いるとデルタ翼に働く抗力が減少し，ボルテックス・フラップを用いた場合とほぼ同等な効果が得られることが示された。しかしながらボルテックス・フラップとボルテックス・プレートを組み合わせた場合には，それらの効果は確認されなかった。

Nomenclature

b Local span

C_r Wing centre-line chord

C_D Drag coefficient

C_{D0} C_D at zero lift

C_L Lift coefficient

C_m Pitching moment coefficient non-dimen-

*Received 1 July, 1992

*[1] Advanced Aircraft Research Group

*[2] College of Aeronautics, Cranfield Institute of Technology, Cranfield, Bedford, MK43 0AL, U.K.

sionalised using Cr and measured about x/Cr = 0.4

Cp Pressure coefficient

g Vortex plate leading-edge position measured from leading-edge of the wing in the chordwise direction

L/D Lift/Drag ratio

$Recr$ Reynolds number based on wing centre-line chord

$U\infty$ Free stream velocity

x Chordwise co-ordinate measured from the apex of the delta wing

y Spanwise co-ordinate orthogonal to x, measured from the wing centre-line

α Wing incidence

α_g Geometrical wing incidence (i.e. without tunnel corrections)

δf Vortex flap deflection angle measured normal to the hinge line

1. Introduction

The leading-edge vortex flap (LEVF) is a full span deflectabe surface at the leading-edge of a delta wing (Ref. 1). With the flap deflected downward, a leading-edge separation vortex may be formed over the forward facing flap surface. (Fig. 1) The suction force generated by the vortex acts on the flap surface and generates a thrust component. Hence the drag is reduced and the lift-drag (L/D) ratio improved. This L/C ratio is an essential factor for the take off and climb performance of delta wing aircraft. Many tests have been made and confirm that the LEVF can improve the low sped aerodynamic efficiency of delta wings. Ref. 2 gives an over-view of LEVF research.

Some earlier tests using a 60° delta wing model with tapered vortex flaps were made at the Cranfield Institute of Technology. (Ref. 3) They showed that the LEVF can increase the L/D ratio by up to 40%, and the L/D ratio is improved over a large range of lift coefficients with little change of trim. It was suggested in Ref. 3 by the second author of this report that the optimum L/D ratio is achieved with the flow coming smoothly onto the deflected LEVF without forming a vortex above or below the flap surface.

The vortex plate proposed in Ref. 4 is similar to a forward facing split flap. This vortex plate is a thin plate attached to the lower surface of the leading-edge of the delta wing. (Fig. 2a) With the plate fitted, a leading-edge cavity is formed between the delta wing and the vortex plate. Ref. 4 suggested that at positive incidence the flow separates at the plate leading-edge and forms a spanwise vortex which induces a suction over the cavity surface. Hence the plate creates some leading-edge thrust and the drag is reduced.

In order to investigate the flow around the

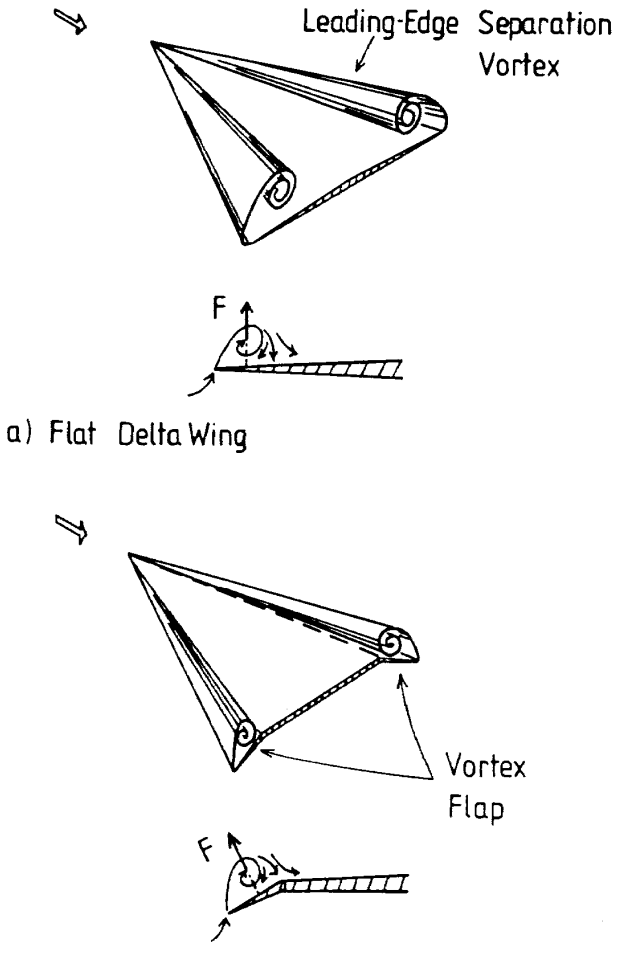

Fig. 1 Concept of Vortex Flap

LEVF at the maximum *L/D* condition and understand how the vortex plate works, a study was made using a 0.53 m span 60° flat delta wing fitted with vortex flaps and vortex plates. It was reported as Part 1 of this study (Ref. 5). The results are summarised below:

a) At the incidence when the *L/D* ratio reaches a maximum, there is only a small separation bubble on the LEVF surface and the flow comes nearly smoothly onto the flap with no large vortex being formed, as was suggested in Ref. 3.

b) At high incidences a leading-edge separation vortex is formed on the LEVF surface. Because of the suction effect of this vortex, the *L/D* is higher than that of the datum wing, as was suggested in Ref. 1.

c) By fitting a vortex plate to the basic wing (no LEVF), the *L/D* ratio for all ranges of C_L greater than 0.3 is significantly improved, because some leading-edge suction acts on the wing. A better performance was obtained with the vortex plate protruding ahead of the leading-edge of the wing. (Fig. 2b)

In Part 1 (Ref. 5), the flat plate wing model which has beveled edges was used. These beveled edges might have affected both the separation position and the formation of the leading-edge separation vortex. Therefore, it is of interest whether conclusions of Part 1 are also applicable to the other wing model which has a different cross section. In this Part 2, further tests are conducted in the 2.4 m x 1.8 m low speed wind tunnel using a 1.15 m span 60° delta wing model. A symmetrical smooth convex shape is used as a cross section of this model, in order to avoid any undesirable separation on the wing surface. This wing model is the same one that was used in Ref. 3. Although the flow condition of the maximum *L/D* was suggested in Ref. 3, the main aim of Ref. 3 was to investigate the benefit of the LEVF. Therefore, it is of use to investigate the flow condition of the maximum *L/D* in detail,

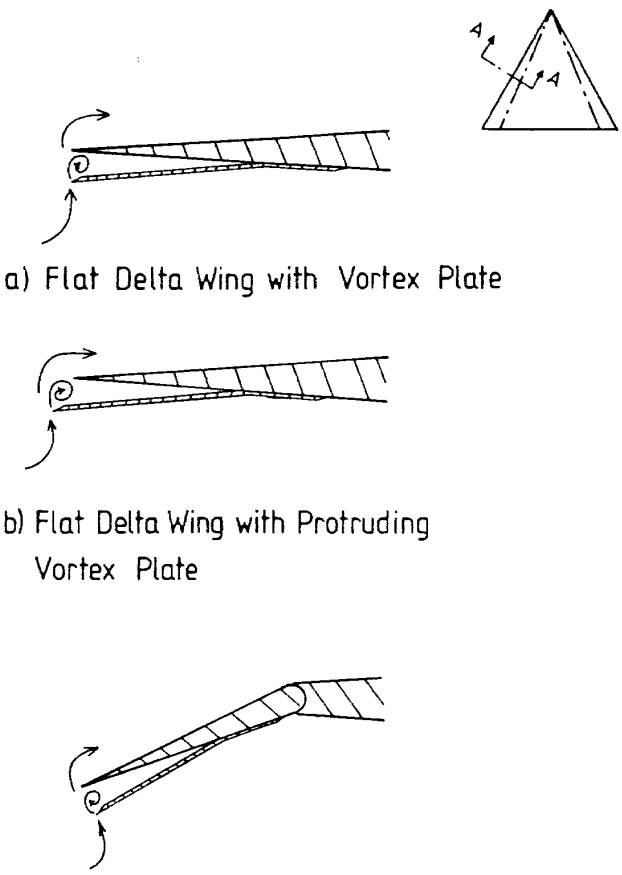

Fig. 2 Concept of Vortex Plate

by using the same model used in Ref. 3.

The previous studies (Refs. 3 and 5) concentrated on incidences up to about 30° because the emphasis was on finding the maximum *L/D* ratios. These values occurred at rather low lift coefficients. Ref. 3 showed that the LEVF was still giving some *L/D* improvement at the highest incidence tested. In practice any benefit at high incidence may be useful.

In Part 1, the vortex plate was attached to the delta wing without flaps deflected. However, when the vortex plate is attached to the deflected vortex flap as is shown in Fig. 2c, the drag reduction will be caused by the effect of combining the vortex flap and the vortex plate. There may be some beneficial effects on wing performance.

In this Part 2, further tests using a delta wing model, whose cross section differs from that of Part 1's model, were conducted to confirm the

conclusions of Part 1. In addition, the effect of high incidences on the LEVF and the benefits of the vortex plate with flaps deflected were also investigated. In summary, the purpose of this Part 2 is

1) to gain more understanding of the complex flows around the delta wing with vortex flaps,
2) to confirm the flow conditions giving the maximum *L/D* ratio of the wing with vortex flaps,
3) to discover whether the LEVF has any benefit at incidences larger than 30°,
4) to investigate the benefits of the vortex plate with flaps deflected.

This research was done at the College of Aeronautics, Cranfield Institute of Technology, U.K., while the first author was staying in the College for a period of one year starting October 1990 with the aid of the S.T.A. research abroad fellowship.

2. Experimental Details

Fig. 3 shows the model details. This model is the same one that was used in Ref. 3. The model is a 60° delta wing with sharp leading-edge and trailing-edges. The centre-line chord length Cr is 1.0 m. The aerofoil section at centre-line is a symmetrical smooth convex shape described by the form:

$$\frac{y}{Cr} = \pm \frac{x}{8Cr}\left(1 - \frac{x}{Cr}\right)\left(1 - \frac{x}{2Cr}\right)$$

The maximum thickness/chord ratio which occurs at 42% Cr is 4.8%. The spanwise

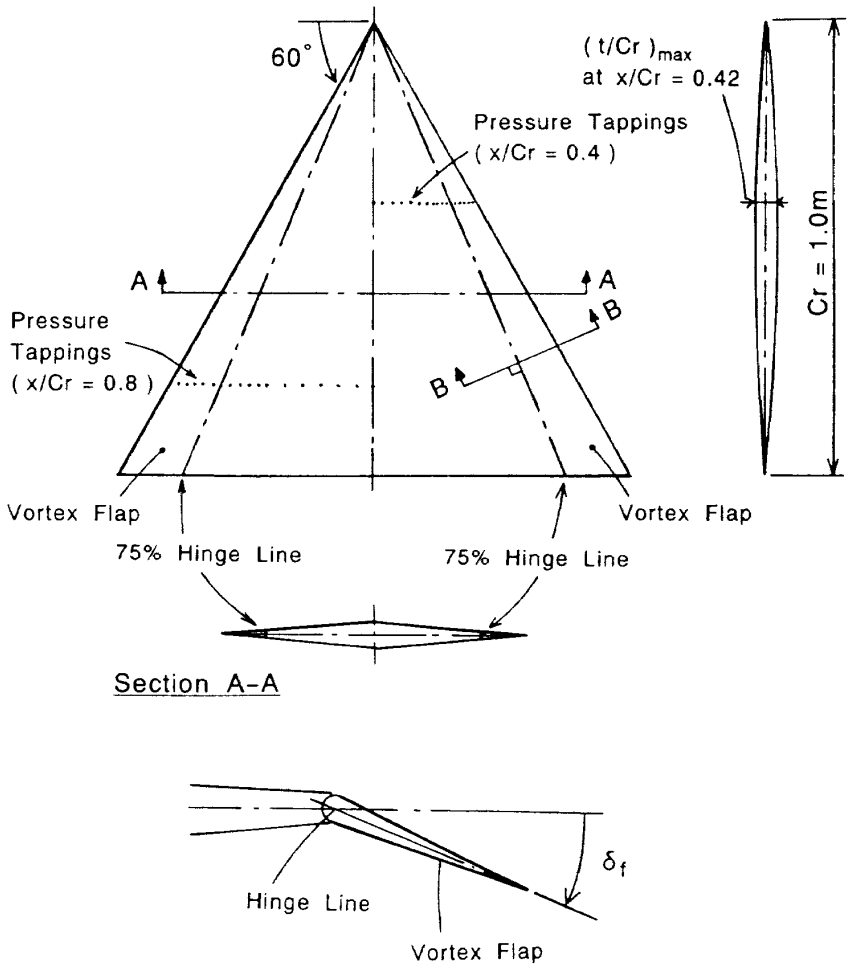

Fig. 3 Delta Wing Model with LEVF

thickness distribution varies linearly from centre-line to tip. The model has two LEVF hinge lines running from the wing apex to 50% and 75% of the trailing-edge semispan station. A thin adhesive tape was attached along the hinge lines to avoid any air flow leak through the hinge line gaps. Two rows of pressure tappings (16 in each row) were located on the upper surface of the right wing at $x/Cr = 0.4$ and the left wing at $x/Cr = 0.8$.

The flap deflection angle δf is defined as the angle formed between the mean line of the inboard wing and that of the LEVF, measured in the plane normal to the hinge line. The sign of δf is positive when the LEVF is deflected downward. Different flap deflections of $\delta f = 0°$ to 60° in 5° increments were tested for 50% and 75% hinge line models in Ref. 3. It was shown that the 75% model has a better performance than that of the 50% model. It was also concluded that the $\delta f = 30°$ case of the 75% model has the best performance for a wide C_L range. Therefore, the tapered LEVF with the hinge lines at 75% semispan was tested in this experiment. In order to check the repeatability of measurements in Ref. 3 and in order to measure the flap performance at high incidences greater than 30°, the datum wing ($\delta f = 0°$) and $\delta f = 30°$ cases were again tested here. Nine different flap deflections of $\delta f = 0°$ to 60° were tested to determine the maximum L/D condition for each flap setting.

Two different types of vortex plate were tested in this experiment. The first type is similar to the one used in Ref. 5. The plan shape at the leading-edge is the same as that of the delta wing model. (Fig. 4a) It is made of 2 mm plate and has a sharp leading-edge. The plate was attached to the lower surface of the datum model (no LEVF deflection). The plate was bent as shown in Fig. 4a so that the distance between the leading-edge of the plate and that of the wing was 10 mm at every spanwise station in side view. The plate can be moved forward, as shown in Fig. 4a. The position of the plate is defined by the chordwise distance (g) between the leading-edge of the wing and that of the vortex plate. In these tests the plate was set at $g/Cr = 0$ and 0.02. The position $g/Cr = 0$ means that the leading-edge of the vortex plate coincides with the leading-edge of the wing in plan view. The vortex plate described above is called the "parallel" vortex plate.

A second type of vortex plate was made in order to check the effect of combining the vortex plate and the vortex flap. The plan shape is smaller than the vortex flap as is shown in Fig. 4b, so that the vortex flap is deflectable. The distance between the leading-edge of the plate and that of the wing in side view is 10 mm at the trailing-edge of the wing. This distance decreases linearly towards the apex of the wing. At the apex this distance is zero. The leading-edge of the plate coincides with that of the wing in plan view. The measurements were done with a flap deflection angle (δf) of 30° and without flaps deflected ($\delta f = 0°$). This vortex plate is hereafter referred to as the "tapered" vortex plate.

The experiments were made in the Cranfield 2.4 m x 1.8 m low speed, closed working section, closed return wind tunnel. All tests were done at a tunnel speed of $U\infty = 30$ m/s. The Reynolds number based on the wing centre-line chord was 2×10^6. The wind tunnel velocity was calibrated and the wind tunnel flow angularity was checked in the empty tunnel before any tests were made. The model was mounted inverted from the overhead balance by a single shielded strut and a tail wire. For measurements over the incidence range of –8° to 32°, the model was mounted at the centre-line of the tunnel. (Fig. 5a) However, it was impossible to set the model at an incidence above 45° in this way. Therefore, an extended centre strut and an extended curved tail strut were used for measurements in the incidence range of 30° to 57°. (Fig. 5b) The model was

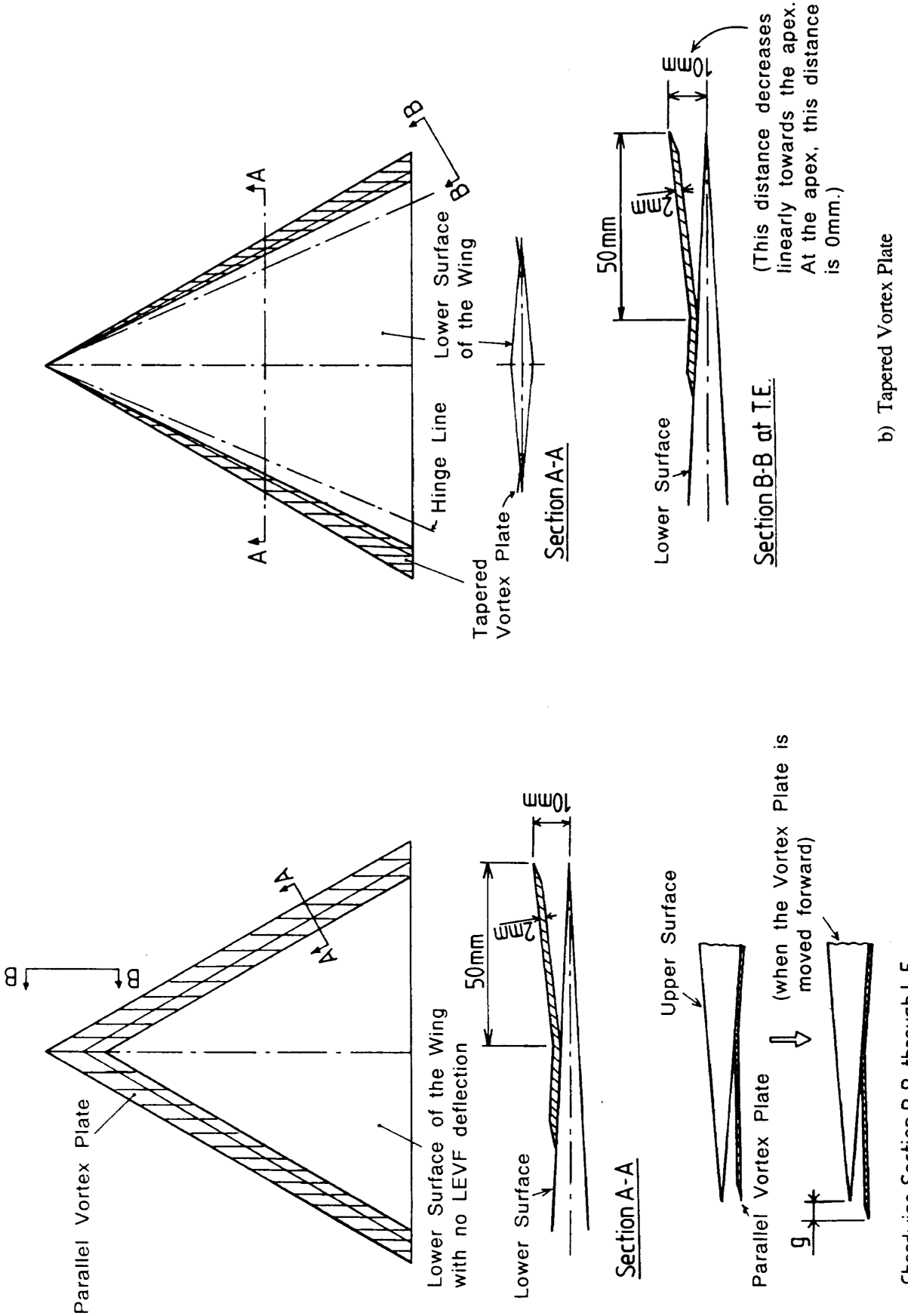

b) Tapered Vortex Plate

a) Parallel Vortex Plate

Fig. 4 Delta Wing Model with Vortex Plate

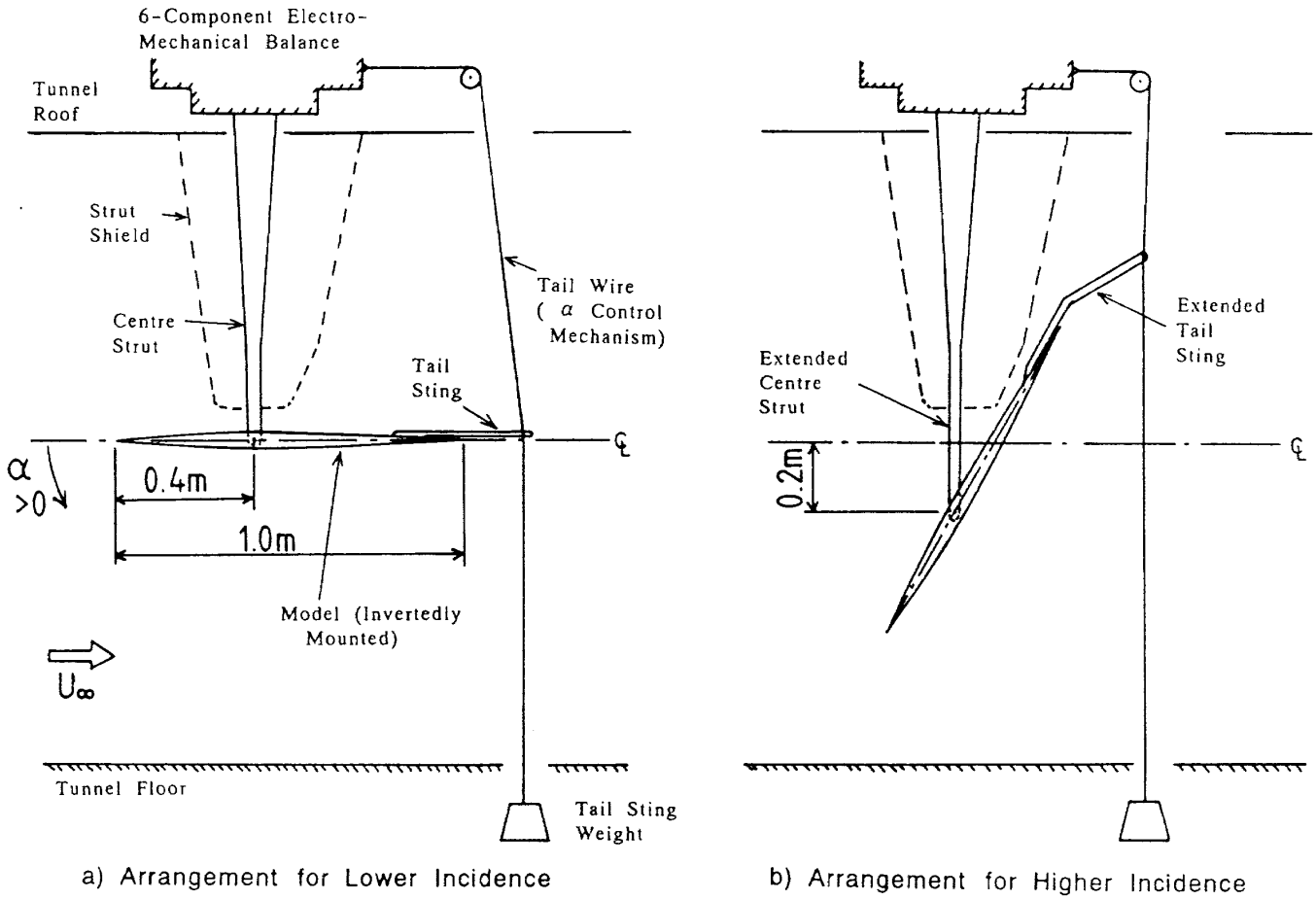

Fig. 5 Wind Tunnel Model Mounting Details

mounted at a position 0.2 m below the centre-line of the tunnel. some pictures of the model mounted in the tunnel are shown in Fig. 6.

Lift, drag and pitching moments were measured using the overhead 6-component electro-mechanical balance and recorded using the tunnel data acquisition system. The strut tare effect was taken into account and tunnel boundary corrections were applied to the measured data. The solid and wake blockage effects were corrected using the approximate method described in Ref. 6. The lift force effect was corrected according to Ref. 7. The effect of static pressure gradient was neglected. Interference between the strut and the model was not accounted for. Since the tunnel boundary corrections used here are only suitable for low incidences, the results obtained here at high incidences must be treated with caution.

In order to measure surface pressure distributions, a "Scanivalve" was mounted within the model. The pressure transducer used was a SETRA Systems model 239 (0.5 psi). This was located immediately outside the tunnel test section. The sampling time at every pressure port was long enough to avoid pressure lag effects. Pressure coefficients (C_p) were calculated based on the undisturbed free stream static pressure. Blockage effects were taken into account for C_p. At the setup for the high incidence, the wind tunnel static pressure measured upstream of the model changed significantly in comparison with the value at low incidence. This was due to the blockage effect of the model and the extended strut. Therefore, a correction of this effect was made to the wind tunnel static pressure in the high incidence configuration.

In many other references, the vortex flap has been attached to the leading-edge of the delta

wing, which causes an increase in model area. It is then difficult to know the precise effect of the vortex flap alone. In our tests, a hinged tapered flap was fitted onto the delta wing without increasing the total wing area. It is then possible to separate out the benefit of the vortex flap and the vortex plate, by calculating the aerodynamic coefficients based on the constant datum delta wing area.

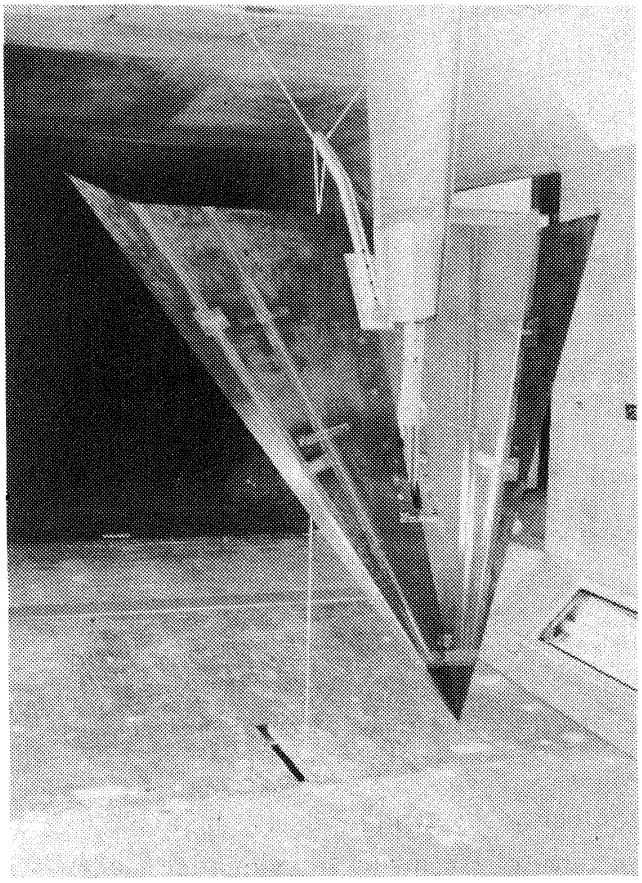

a) Model with $\delta f = 30°$ at a = 57°

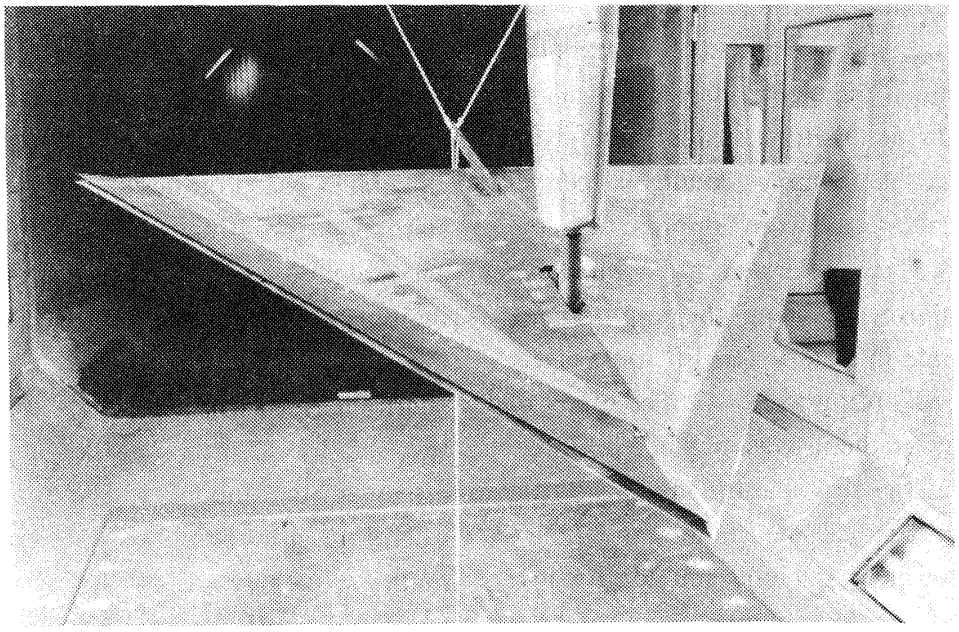

b) Model with the parallel vortex plate

Fig. 6 Delta Wing Model and Wind Tunnel

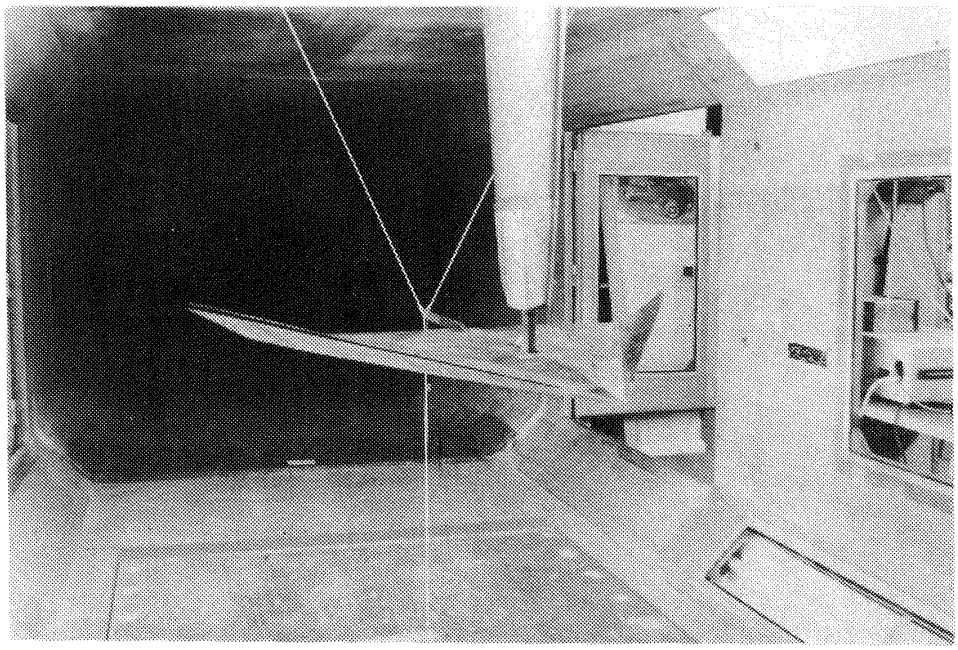

c) Model with the tapered vortex plate at $\delta f = 30°$

Fig. 6 (Continued)

3. Results

3.1 Vortex Flap

Measurements for the datum wing and for the $\delta f = 30°$ case were done over an incidence range of –8° to 57°. The previous force and moment results in Ref. 3 (which were made at incidences up to 30°) and the present results in the same incidence range, agree well.

3.3.1 Lift

Fig. 7 shows the C_L vs. α curves for the datum wing and the $\delta f = 30°$ case. Results which were obtained using the low incidence rig and the high incidence rig are shown in the same figure. The two sets of results connect 'smoothly' at about $\alpha = 30°$. At zero incidence, the C_L of the datum wing is slightly negative. Since the model is symmetrical, the C_L should be zero. The symmetry of the datum wing model was carefully checked and found to be good. The reason why the C_L showed a negative value at $\alpha = 0°$ is thought to be due to the presence of the shielded strut.

Fig. 7 shows that deflecting the LEVF downwards moves the whole $C_L - \alpha$ curve to the right. Thus the zero lift incidence and the stall angle are increased while the C_L at a constant incidence (below the stall) is reduced.

3.1.2 Drag

The $C_D - \alpha$ curves (Fig. 8) show the same trend, the whole curve being moved to higher values of incidence.

3.1.3 Lift/Drag Ratio

Fig. 9 shows the lift to drag ratio (L/D) versus C_L. The $(L/D)_{max}$ for a flap deflection of 30° is increased from the datum wing value 10.4 to 11.3. For the datum wing, the L/D at negative lift is higher than that for positive lift. Again any lack of symmetry is probably due to strut interference. In order to visualise the LEVF deflection effects on L/D more clearly, the percentage increase in L/D is plotted in Fig. 10. This shows that the L/D is increased above that of the datum wing for lift coefficient between 0.2 and 1.2. The greatest percentage improvement is about 40% at a C_L of 0.45, which agrees with the results of Ref. 3. However, after the stall the $\delta f = 30°$ tests show that there is no benefit in using the LEVF.

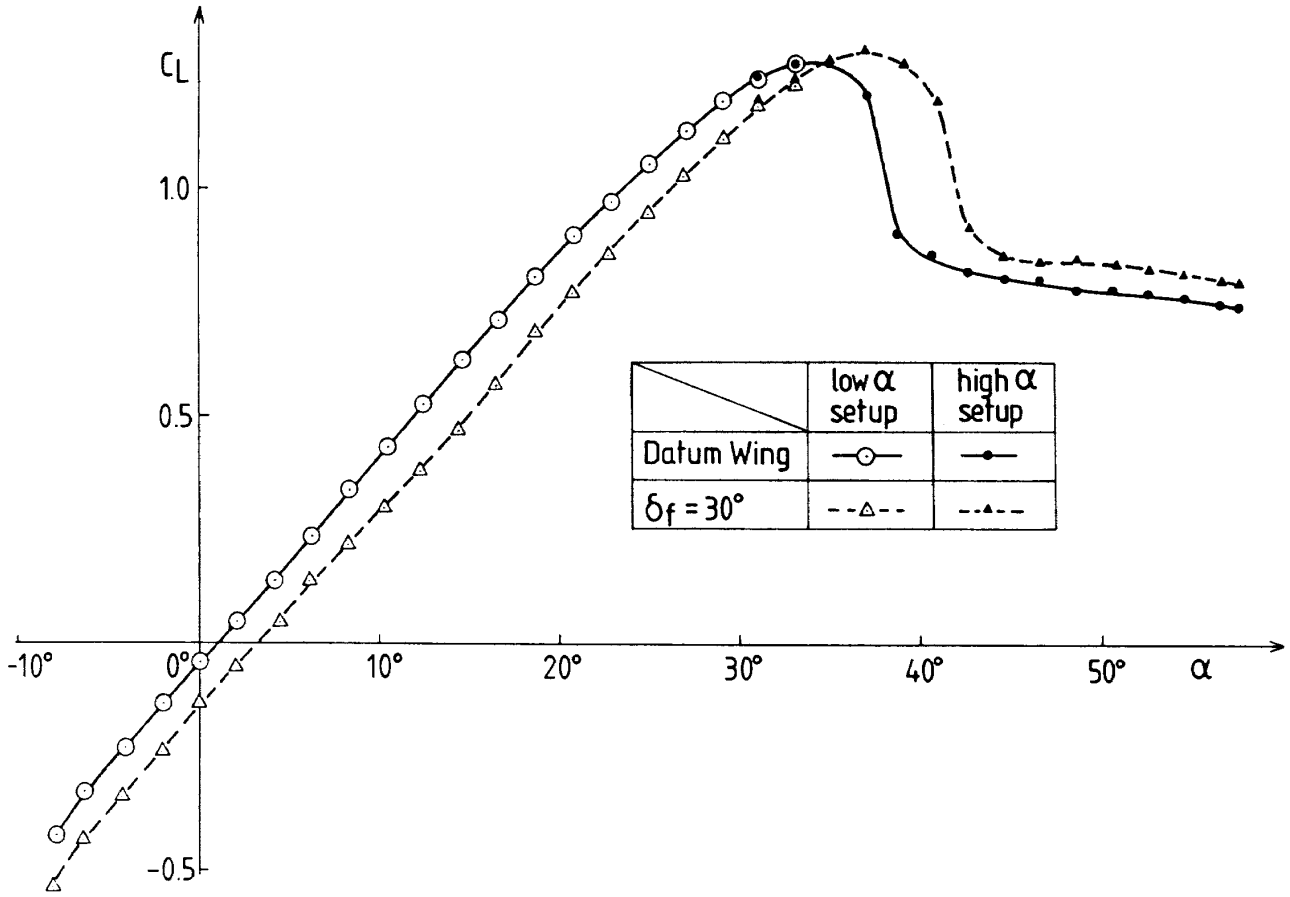

Fig. 7 Effect of LEVF on C_L vs. α

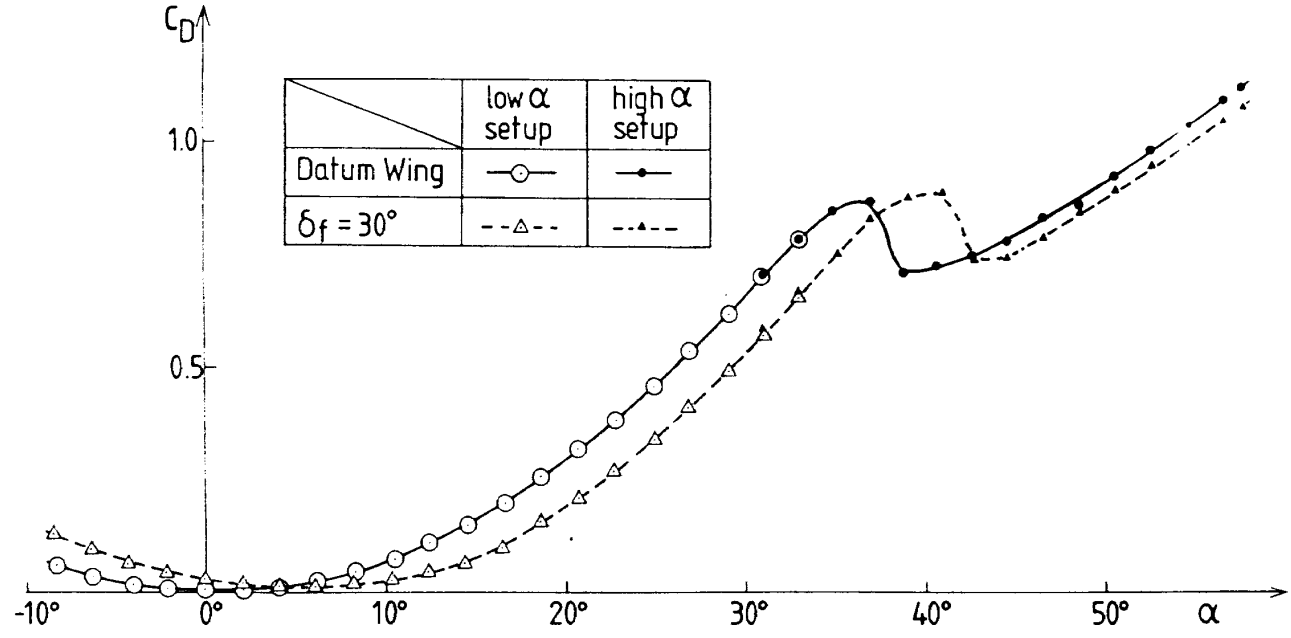

Fig. 8 Effect of LEVF on C_D vs. α

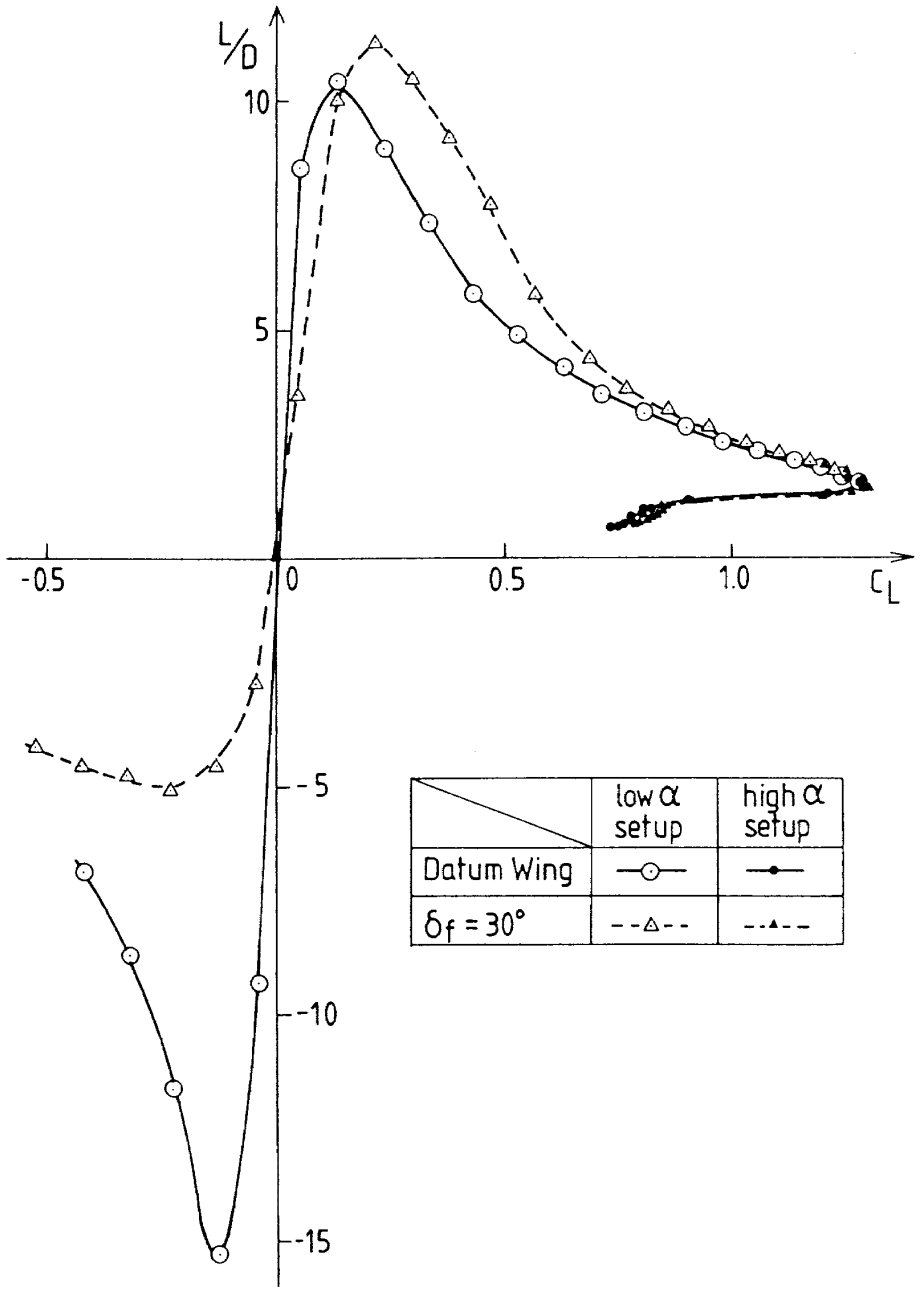

Fig. 9 Effect of LEVF on *L/D* vs. *CL*

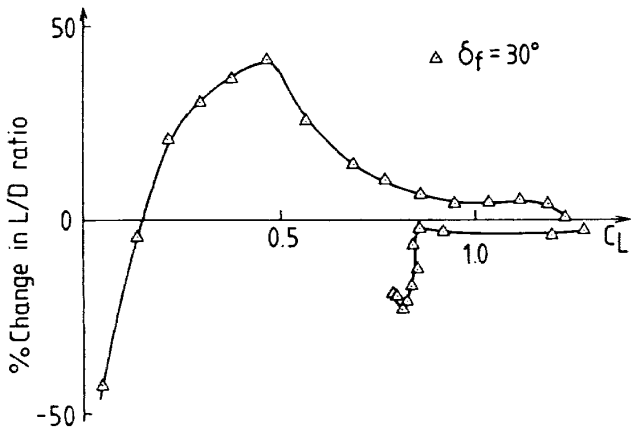

Fig. 10 Effect of LEVF on *L/D* improvements

3.1.4 Pitching Moment

Fig. 11 shows the pitching moment curves measured about the model mounting point x/Cr = 0.4 for all tests including the vortex plate results. The LEVF has little effect on Cm. The $Cm - CL$ curves are roughly linear before the stall and Cm values at CL = 0 are zero for both cases. The aerodynamic centre position measured from the $Cm - CL$ slope is 0.57 Cr for both cases. These results coincide with those of Ref. 3.

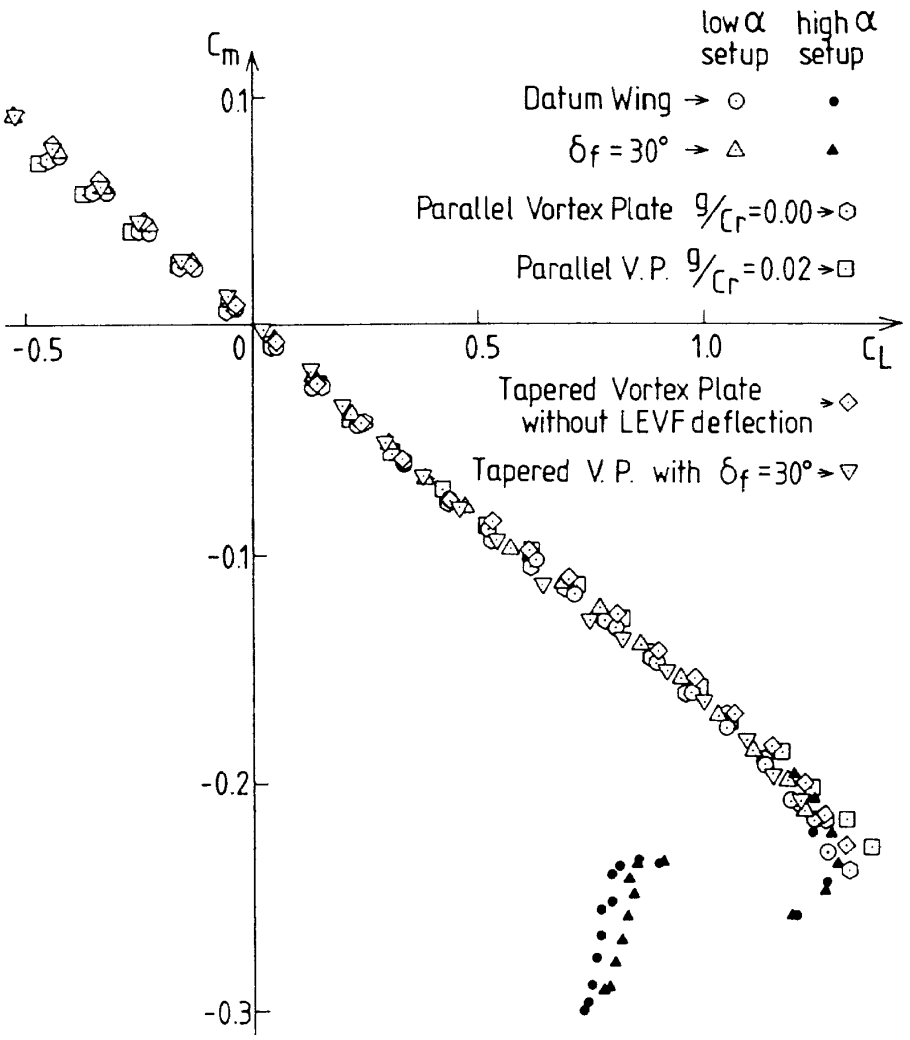

Fig. 11 Effects of LEVF & Vortex Plate on *Cm* vs. *CL*

3.1.5 Pressure Distributions

Figs. 12 (datum wing) and 13 ($\delta f = 30°$) show surface pressure distributions for the upper surface at $x/Cr = 0.4$ and 0.8. Although the measurements were done at the same conditions as in Ref. 3, the results show significant differences. In order to find out the reason, some pressure measurements were repeated in the Cranfield 2.4 m x 1.2 m low-speed wind tunnel. The condition of the pressure tappings and the pressure tubes inside the model were checked. Test methods, including the pressure sampling time, were checked. Results similar to the present results were obtained. Therefore, it appears that pressure measurements reported in Ref. 3 are inaccurate. Further investigations suggest this was due to leaking pressure tubing.

Fig. 12a shows that Cp distributions at $x/Cr = 0.4$ for the datum wing. At $\alpha = 3.1°$, there is already a small suction region in the tip area, which may be a small separation bubble rather than a leading-edge separation vortex. At $\alpha = 6.2°$ the features of a leading-edge separation vortex are clearly recognisable. There is a flat Cp area at the tip of the wing which shows the existence of a secondary separated flow. At $\alpha = 15.6°$, 18.7° and 24.9° there is a large leading-edge separation vortex on the wing with high peak suctions. By $\alpha = 37.0°$ the Cp distribution shows that the vortex suction has decreased but spread out to cover half the local wing span. This may signify vortex breakdown. At incidences greater than 42.7°, the Cp distributions is completely flat. This suggests that the vortex type of flow has collapsed and that the flow is now totally separated over the top surface of the wing.

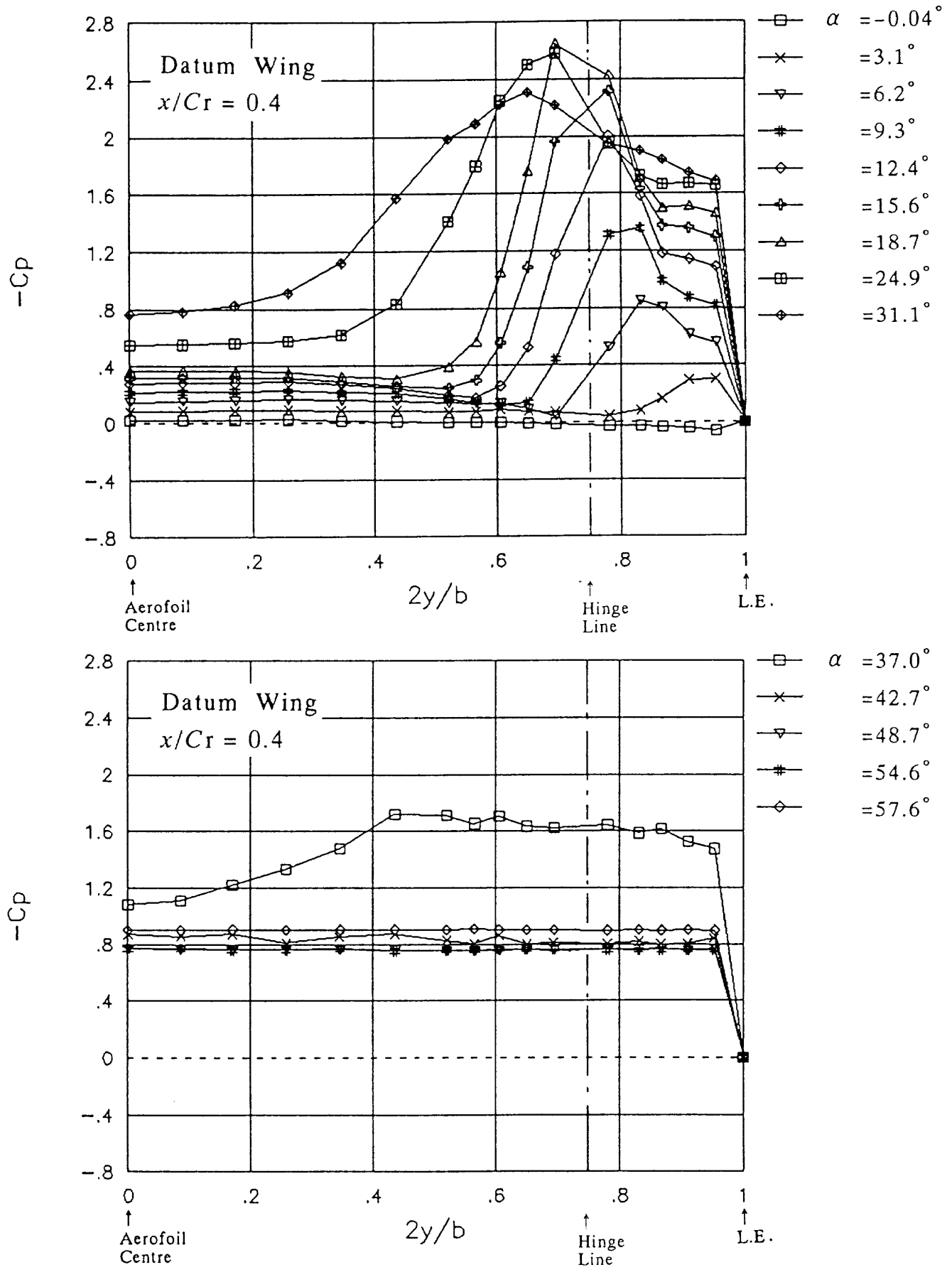

a) $x/C_r = 0.4$

Fig. 12 Surface Pressure Distributions (Datum Wing)

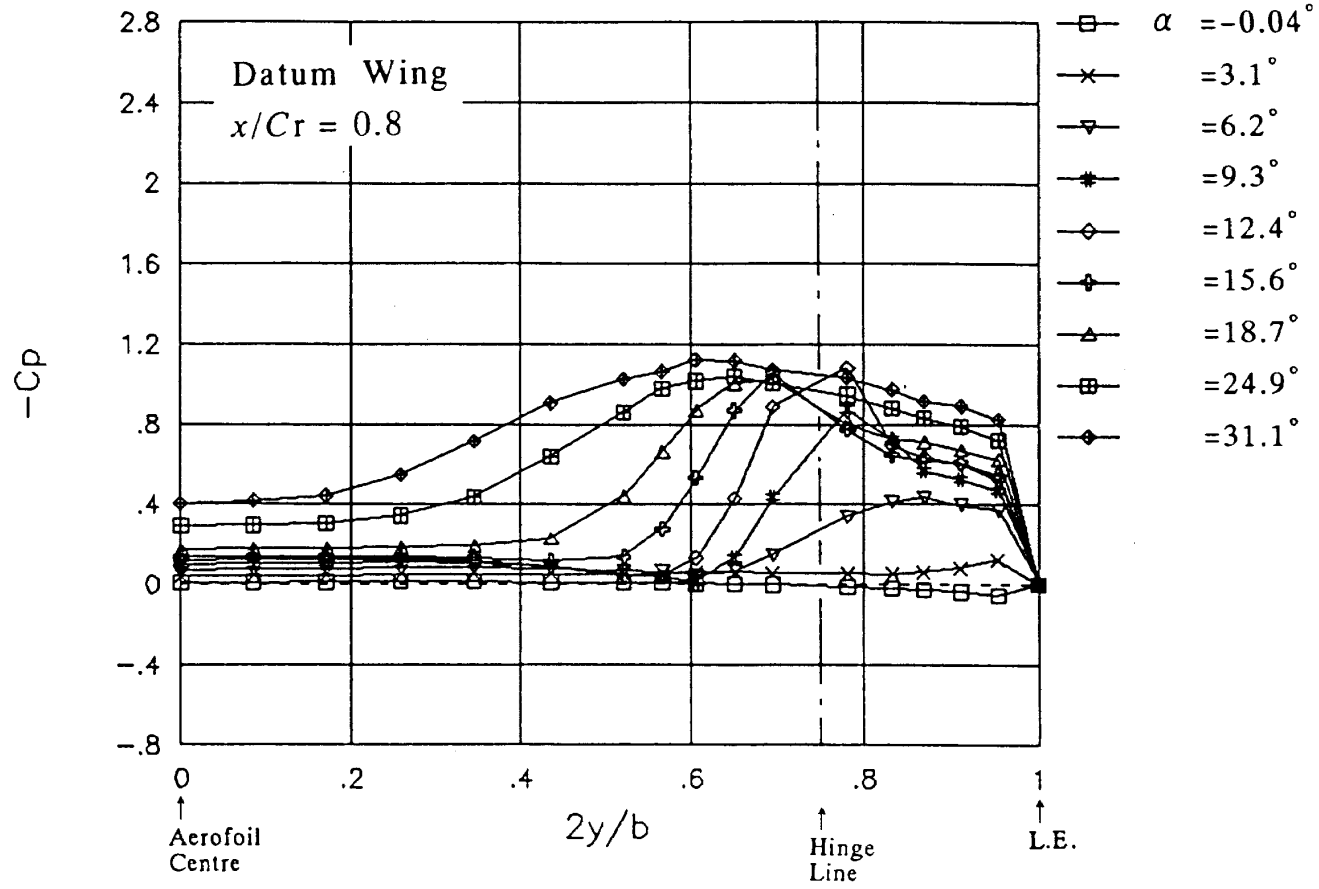

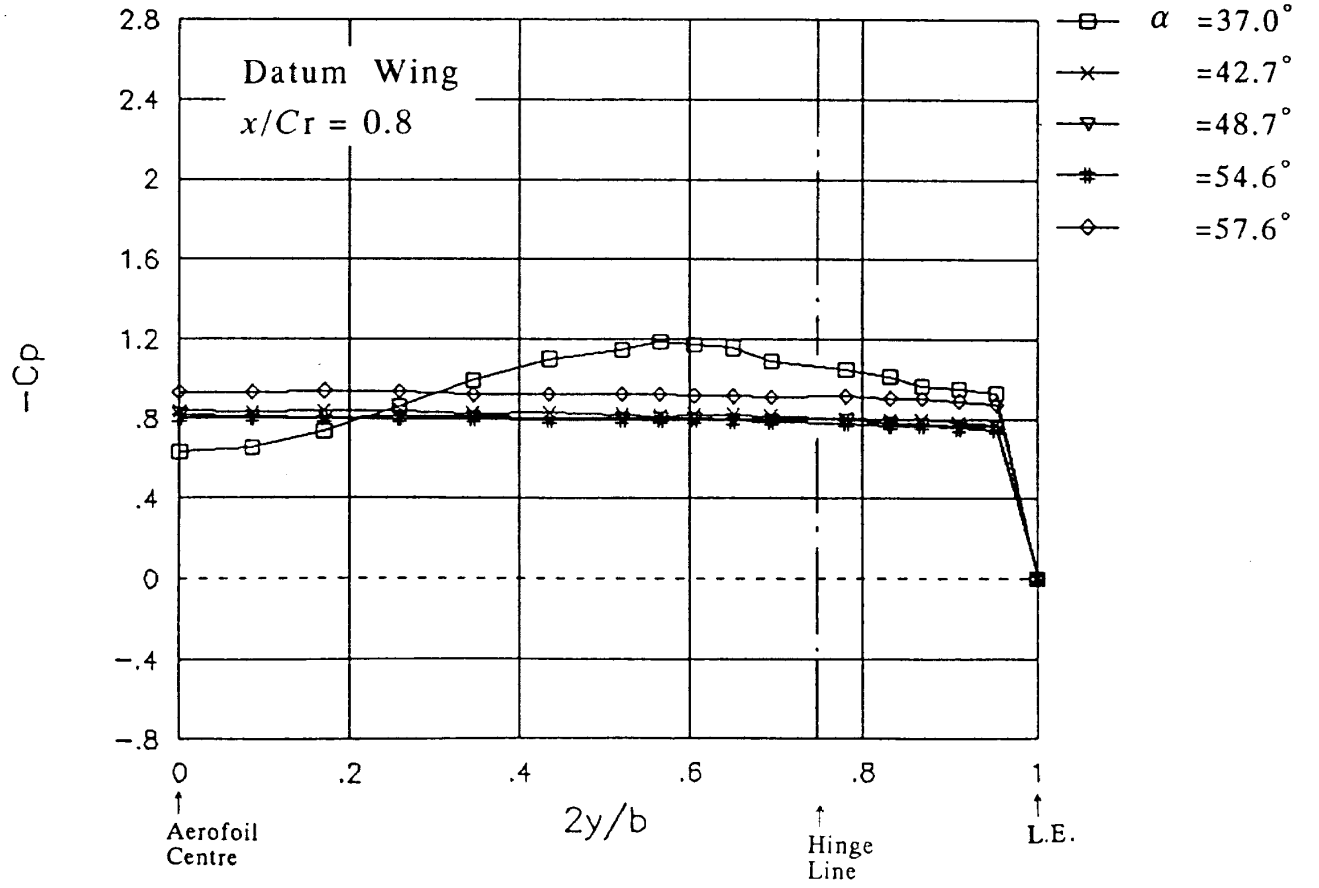

b) $x/Cr = 0.8$

Fig. 12 (Continued)

Fig. 12b shows the C_P distributions at x/C_r = 0.8 for the datum wing. Although the peak values are smaller than those at x/C_r = 0.4, the C_P distributions at low incidence are similar to those at x/C_r = 0.4. According to Ref. 8, the vortex breakdown position for flow over a flat delta wing moves forward as the incidence increases, and reaches the wing trailing-edge at about α = 15°. The data in Ref. 8 suggest that for $\alpha \geq 20°$ vortex breakdown has occurred at x/C_r = 0.8 and this would explain why no high suction peaks are achieved at high incidences at this station.

Fig. 13a shows the C_P distributions at x/C_r = 0.4 for the wing with δf = 30°. At α = 6.1°, there is no sign of vortex formation and this suggests that the flow comes smoothly onto the flap surface. At α = 9.2°, a small separation is seen on the flap. At α = 15.5°, there are signs of a secondary separation inside the leading-edge separation vortex. The spanwise length of the vortex at α = 12.3° and 15.5° is almost the same as the flap span. At α = 24.8°, the suction caused by the vortex reaches its maximum value. After the stall ($\alpha > 37.1°$), the C_P shows a flat distribution suggesting that the flow has totally separated from the wing surface. Therefore there was no benefit in L/D results for the δf = 30° case after stall. (Fig. 9)

Fig. 13b shows the results at x/C_r = 0.8 for the δf = 30° case. It is noted that the flow comes smoothly onto the flap at incidences between 6.1° and 9.2°.

Figs. 14a and b show some C_D vs. C_L curves together with the corresponding flow pattern sketches in the transverse plane x/C_r = 0.4. These sketches were deduced from the surface pressure measurements. (Figs. 12 and 13) The point where the L/D attains its maximum value is also marked. Near this point the flow patterns show that there is either a small separation region on the wing (at α = 3.1° for the datum wing, Fig. 14a and at α = 9.2° for the δf = 30° case, Fig. 14b) or that the flow comes smoothly onto the wing surface (at α = 6.1° of the δf = 30° case, Fig. 14b). The conditions at the $(L/D)_{max}$ point will be discussed in detail in Section 3.2.

3.1.6 Comparison with Other Experiments for the Flat Delta Wing

In this section, some comparisons are made with other experimental results from tests on flat delta wings. In Ref. 9, measurements were made at a Reynolds number of 0.48 million (based on the root chord), using a 0.27 m span 60° delta wing with a 6% plano-convex section. The incidence range was 0° to 60°. In Ref. 10, measurements were made at a Reynolds number of 2.37 million using a 0.92 m span 60° delta wing. This model had a 12% biconvex section, which is quite similar in shape to that of the present model. Incidences up to 38° were tested.

Fig. 15 shows the C_L vs. α curves for the datum wing, the 6% plano-convex wing and the 12% biconvex wing. The 6% plano-convex wing data shows a 'bump' at an incidence of about 12°. The reason for this was not identified in Ref. 9. Apart from this 'bump' and the difference of zero-lift incidence, the results of the present datum wing and the plano-convex wing show similar C_L distributions, even after the stall occurs. The results from the 12% biconvex wing tests are very similar to those of the datum wing tested here.

Fig. 16 shows the C_D vs. α curves for the three wings. The results from the 6% plano-convex wing are quite similar to the present results for the whole incidence range including the post stall region. The 12% biconvex wing shows larger C_D values than the other two wings at low incidences but this difference is reversed at the higher incidences. Drag is known to be sensitive to the section profile.

3.2 The Effect of δf on L/D at Constant Incidence

In order to find the condition which gives the maximum L/D, some measurements were made by changing the flap deflection angle δf at constant incidence. Flap angles were varied between 0° and 60° at fixed incidence values of 6°, 8°, 10°, 12° and 14°. Force measurements and upper surface pressure measurements were made under these conditions. At α = 6° and 12°, the lower surface

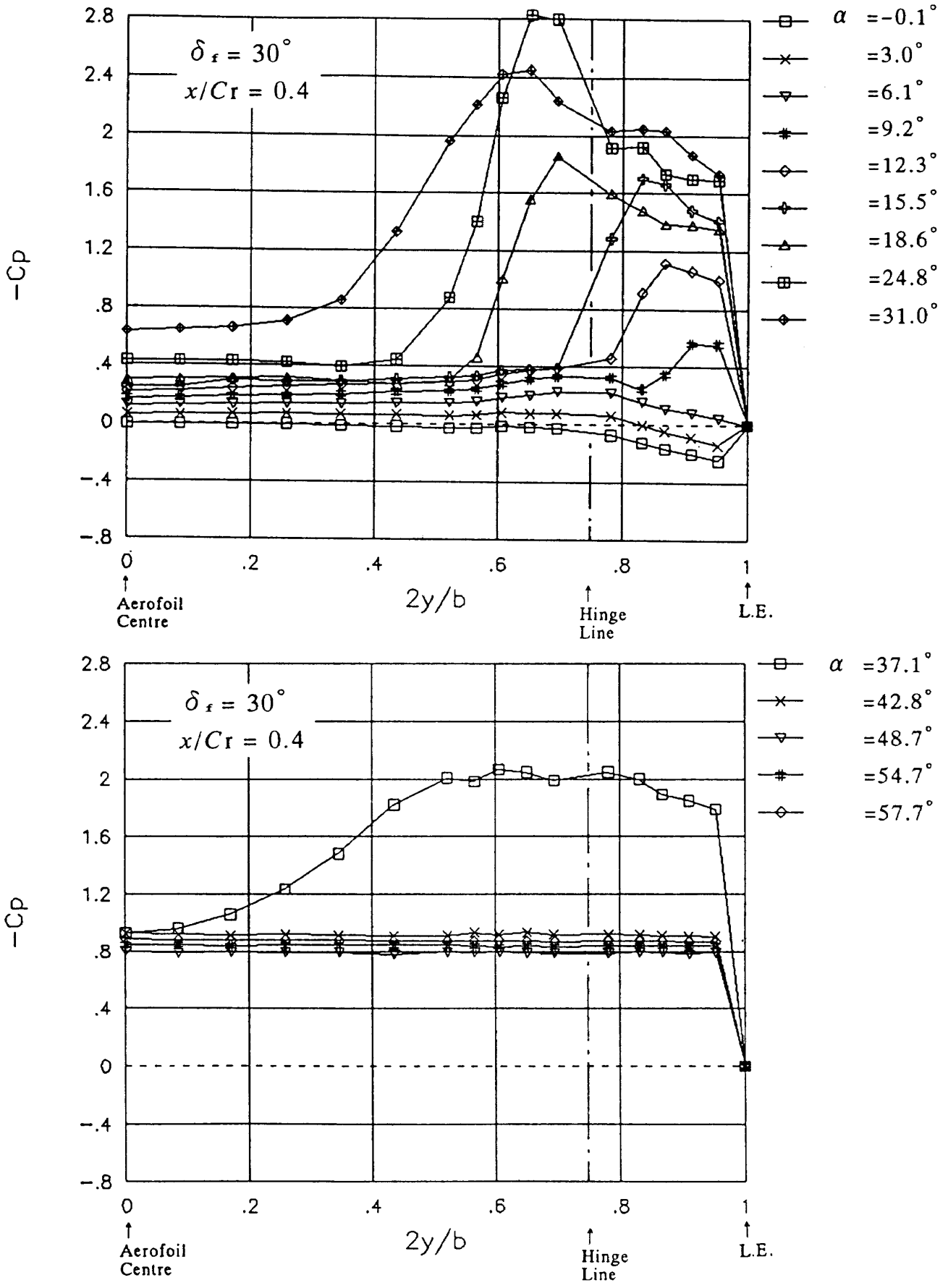

a) $x/Cr = 0.4$

Fig. 13 Surface Pressure Distributions (δf=30°)

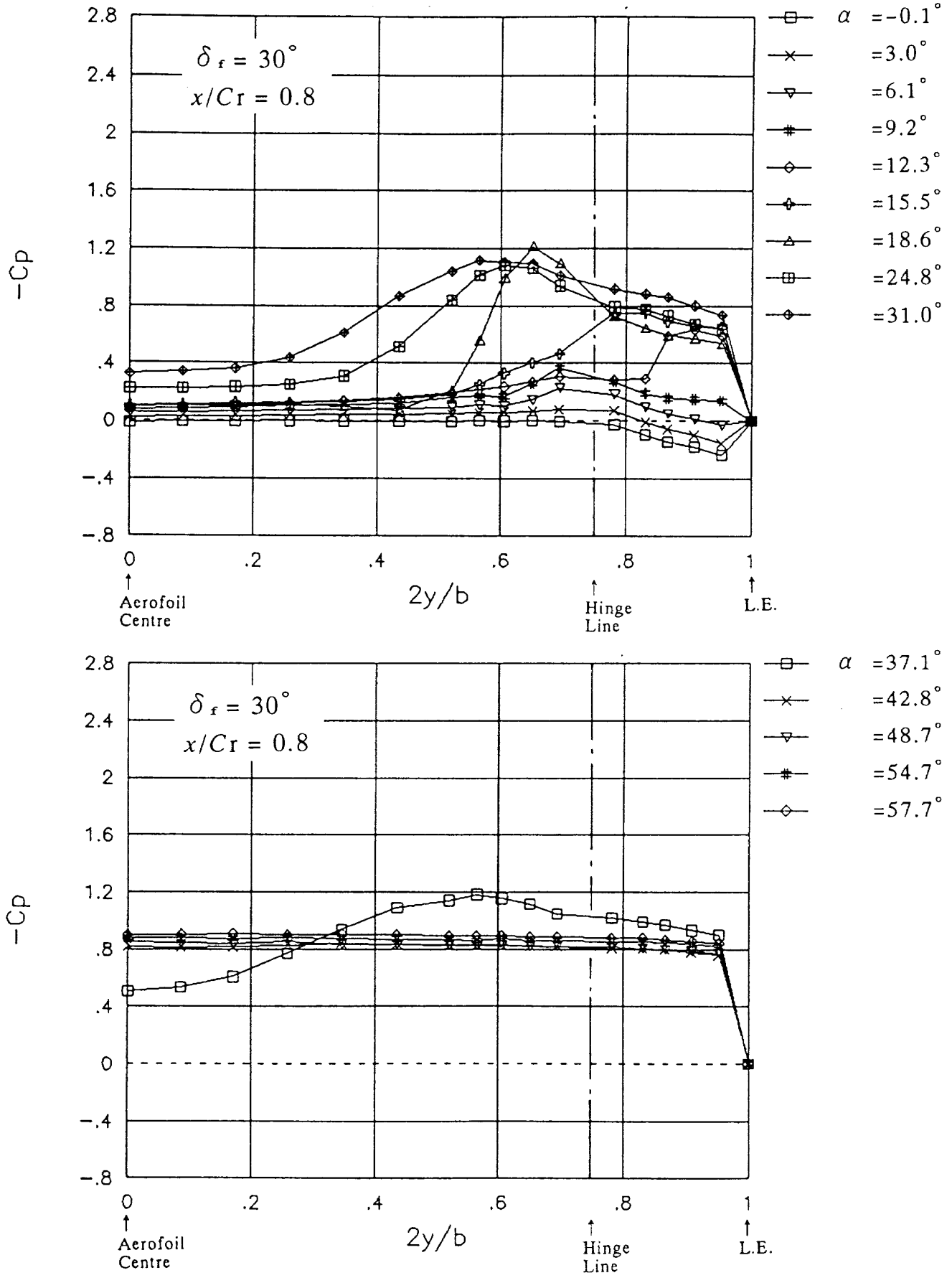

b) $x/Cr = 0.8$

Fig. 13 (Continued)

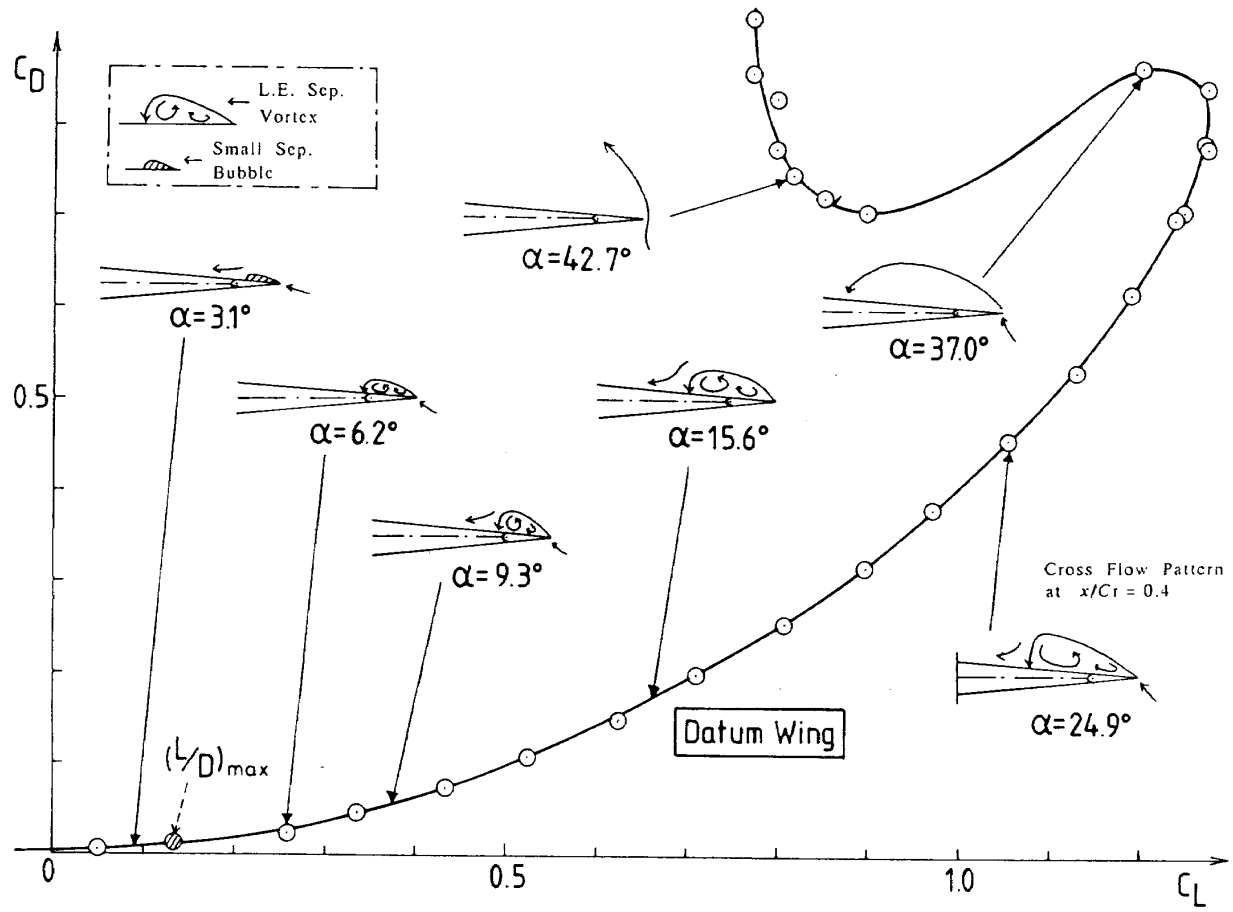

a) Datum Wing

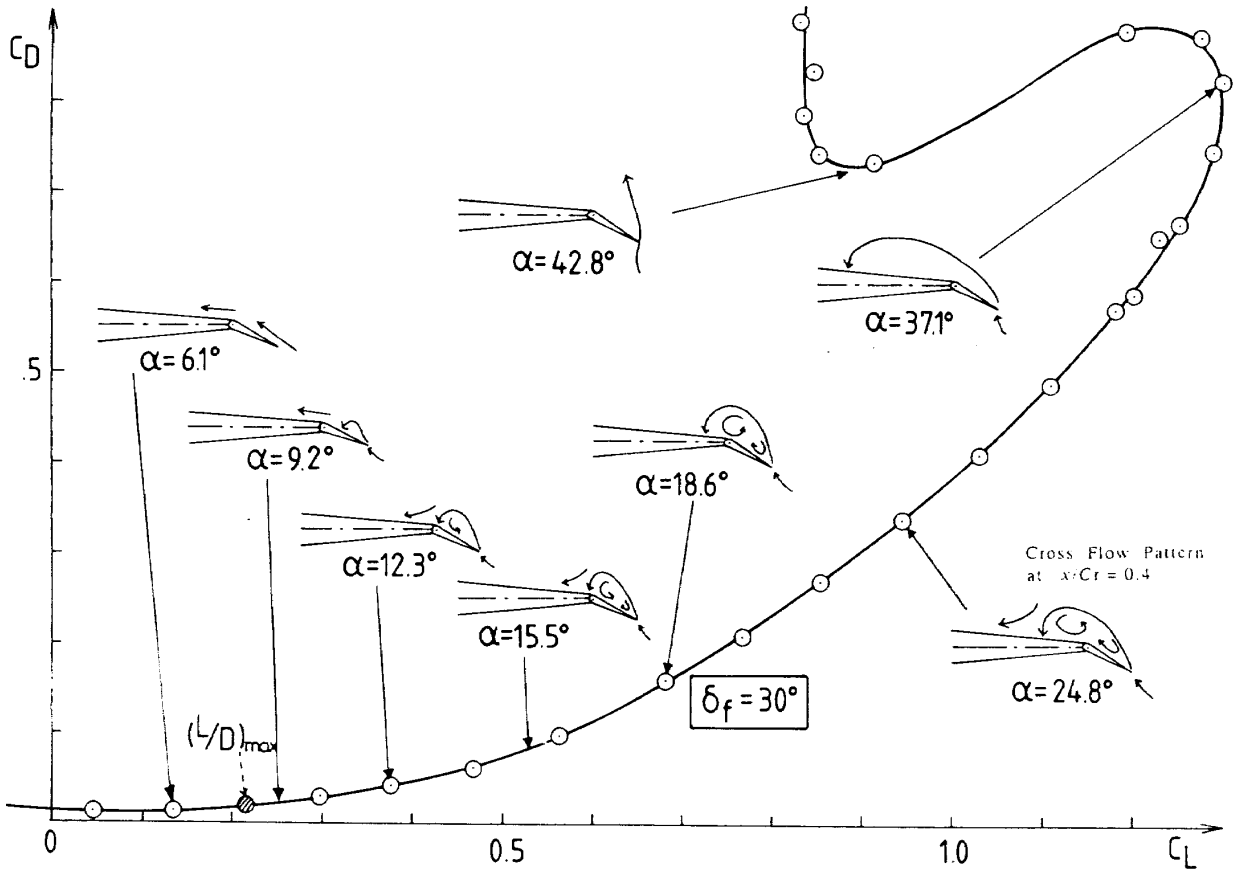

b) $\delta_f = 30°$

Fig. 14 C_D vs. C_L and Cross Flow Patterns

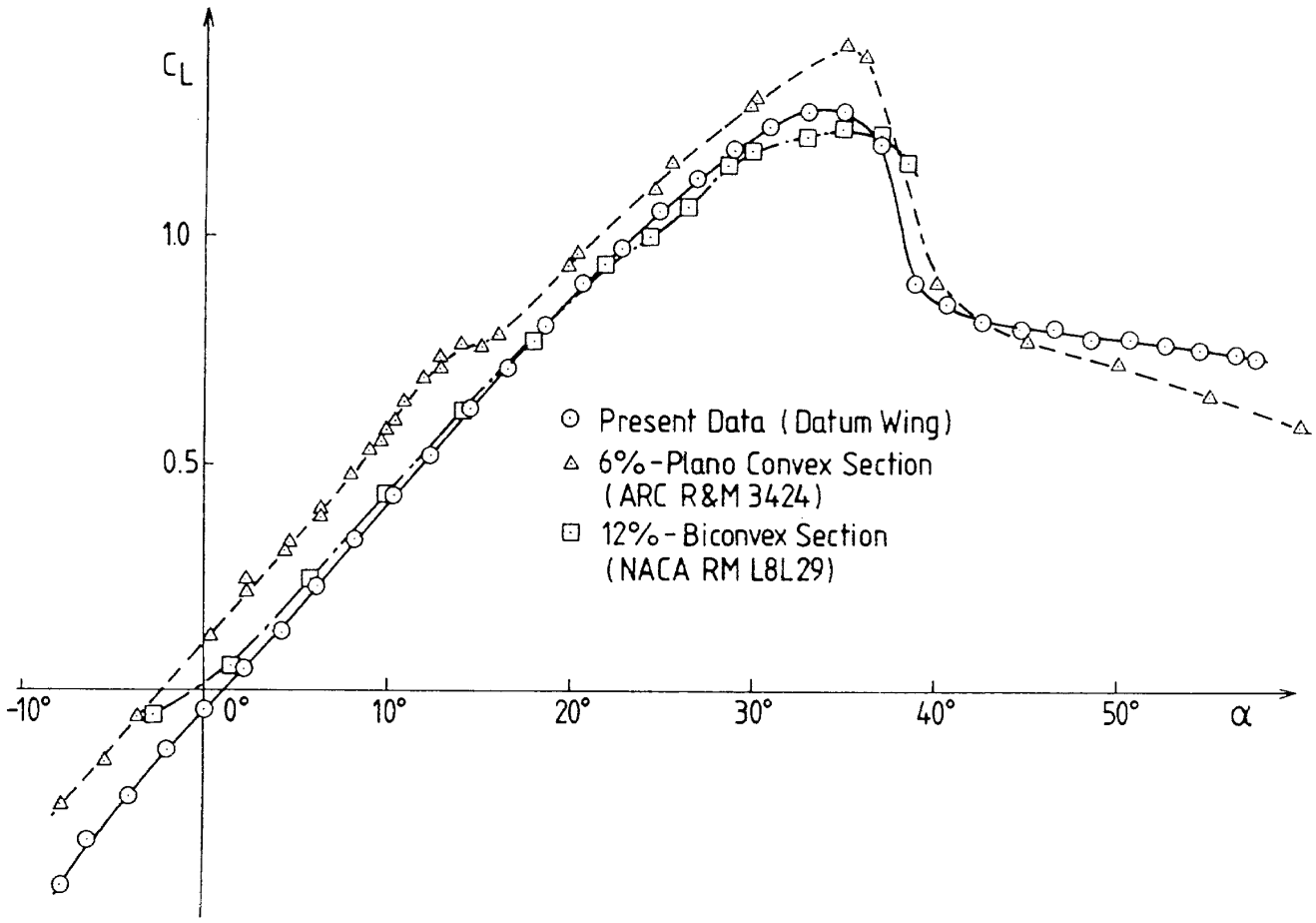

Fig. 15 Comparison with Other Experiments (C_L vs. α)

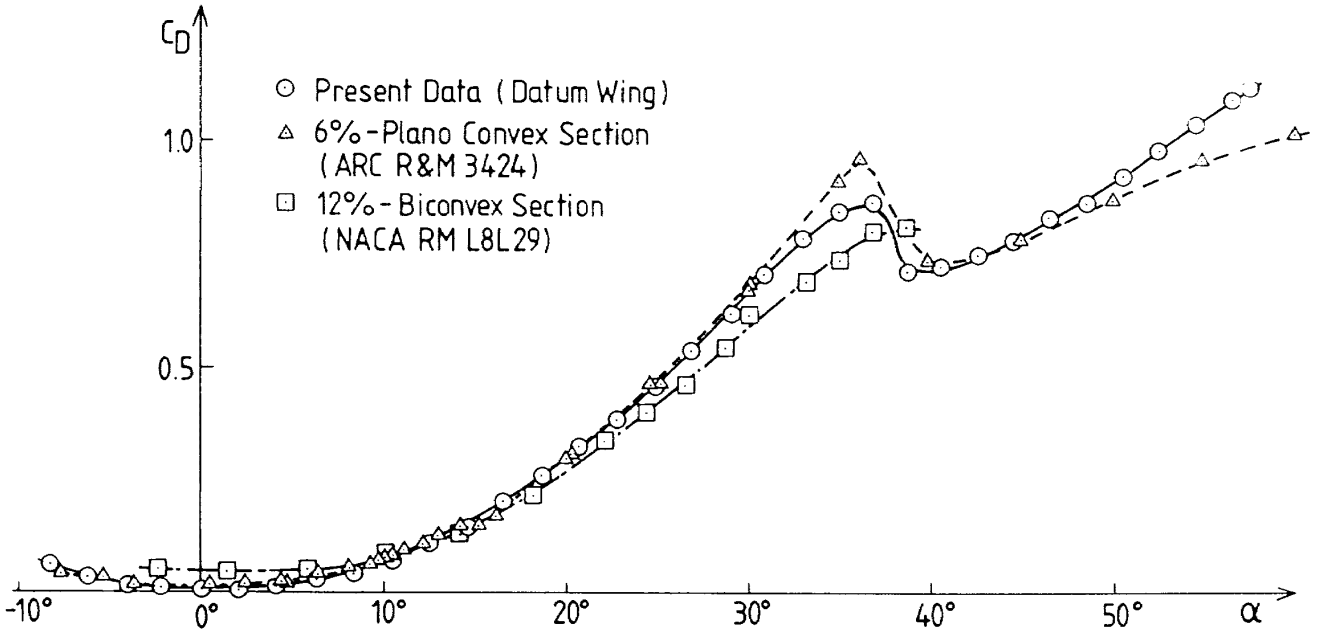

Fig. 16 Comparison with Other Experiments (C_D vs. α)

pressure distributions were also measured. The incidences, as corrected for tunnel wall interference, are different for every flap deflection angle. However, these differences are quite small. Therefore, the geometrical incidence α_g as measured from the tunnel centre-line is used in this section to define the incidence angle.

3.2.1 Lift/Drag Ratio

Fig. 17 shows L/D versus δf at different incidences. This shows that at α_g = 6° the L/D attains a maximum with δf = 20°. As the incidence increases, the maximum L/D decreases and the δf at which $(L/D)_{max}$ is achieved increases. For example, the $(L/D)_{max}$ at α_g = 12° is about two thirds of that at α_g = 6° and is attained at δf = 30°.

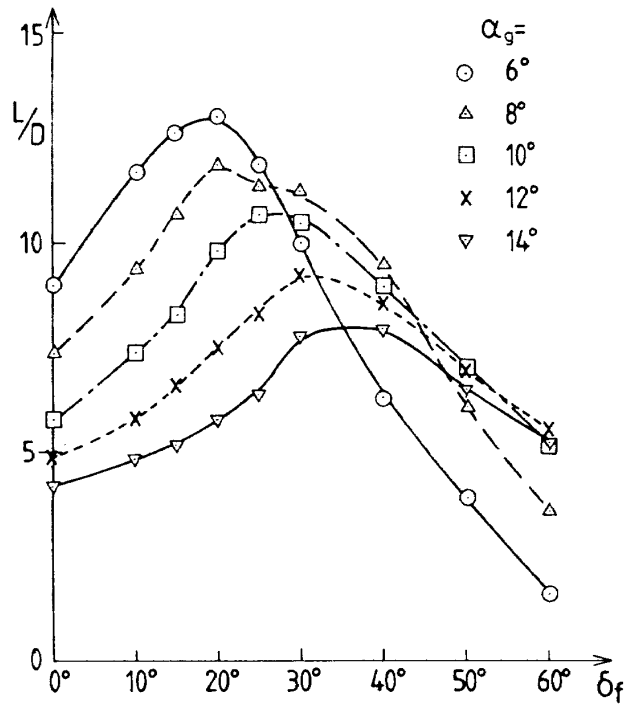

Fig. 17 L/D vs.δf at Constant α_g

3.2.2 Pressure Distribution

Figs. 18a) – e) show measured pressure distributions together with the corresponding flow pattern sketches in the transverse plane. These sketches were deduced from the pressure measurements. Different δf results (at constant α_g) are shown in each figure. Results obtained at x/Cr = 0.4 are shown on the left hand side of each figure and those at x/Cr = 0.8 on the right hand side. The flap deflection angle at which the L/D attains its maximum value (and the corresponding incidence) is also marked.

Figs. 18 show there are small differences between the x/Cr = 0.4 and 0.8 results. The suction peak of the pressure at x/Cr = 0.8 is usually smaller than that at x/Cr = 0.4. However, the spanwise shapes of the Cp distributions are quite similar.

At α_g = 6° (Fig. 18a), the L/D attains its maximum at δf = 20°. At this flap deflection angle there is a small suction region at the leading-edge of the upper surface at x/Cr = 0.4 or no leading-edge suction peak at x/Cr = 0.8. This means that only a small separation region is formed at x/Cr = 0.4 and the flow comes smoothly onto the upper flap surface at x/Cr = 0.8. On the lower flap surface at δf = 20°, there is no separation at either x/Cr position. At δf = 25°, there is no separation region on either surface at either of the x/Cr stations.

At α_g = 6°, as the flap deflection angle δf decreases below δf = 20°, so the spanwise length of the separation bubble on the top surface increases. At δf = 0° there is a sign of secondary separation on the upper surface and a leading-edge separation vortex has formed over the wing.

As δf increases beyond 20°, so separation occurs at the flap hinge line and a separation region is formed inboard of that line (see e.g. δf = 40°). Further increase of the flap angle causes the flow to separate at the leading-edge of the lower surface (e.g. δf = 50° and 60°).

Fig. 18b (α_g = 8°) shows similar results to those of Fig. 18a, but there is no clear indication of where or whether the flow comes smoothly onto the LEVF surface. Fig. 18c (α_g = 10°) shows that the suction on the flap at a given δf is much higher than that at α_g = 8° and it is seen that a stronger vortex is formed on the flap surface.

At α_g = 12° (Fig. 18d), the L/D attains its maximum at δf = 30°. At this flap deflection angle the leading-edge separation vortex is formed on the flap upper surface and its reattachment line almost coincides with the flap hinge line (as was also shown in Fig . 13a). As δf decreases below δf = 30°, the spanwise length of the separation vortex increases

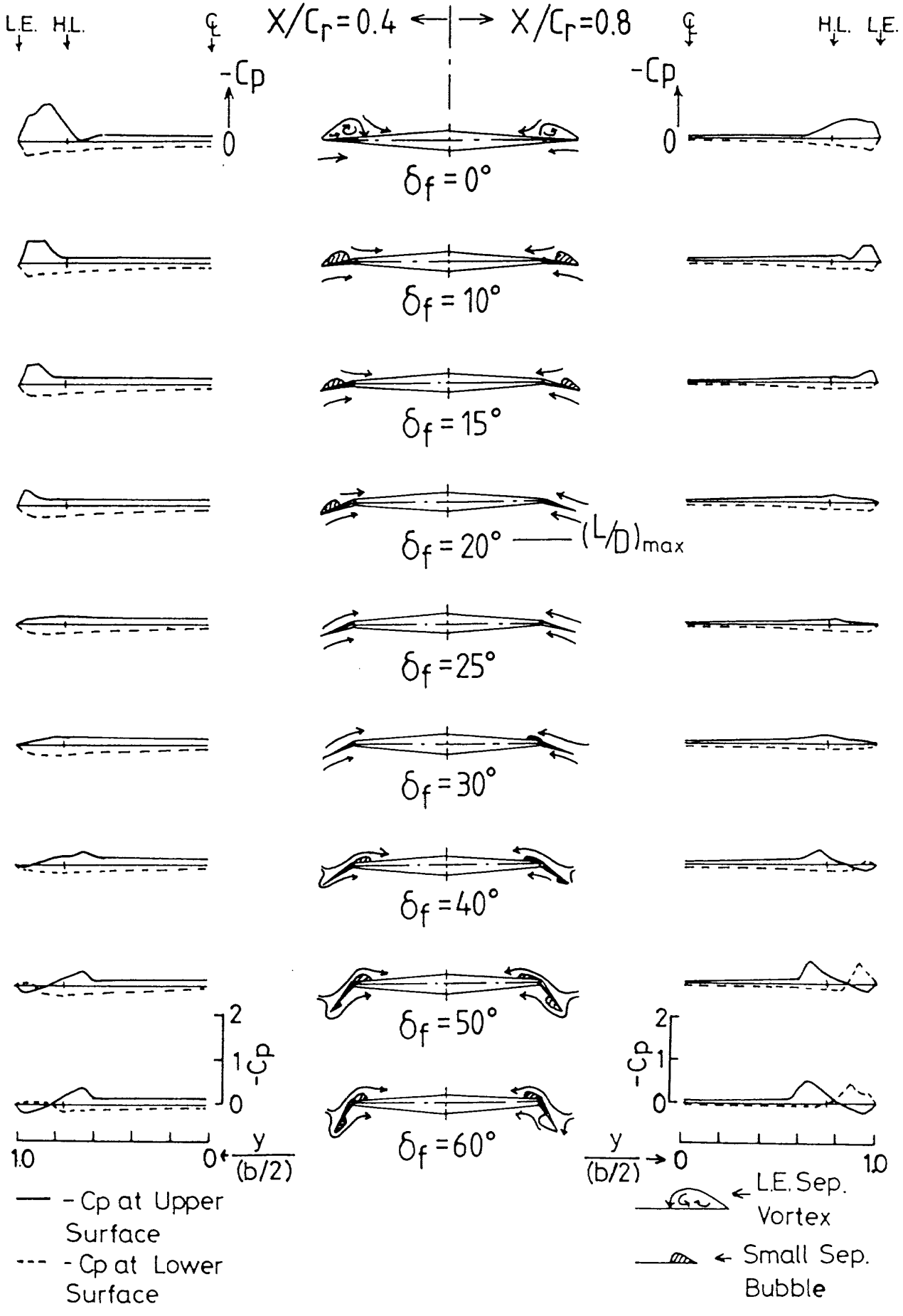

a) $\alpha_g = 6°$

Fig. 18 C_p and Cross Flow Patterns at Constant α_g

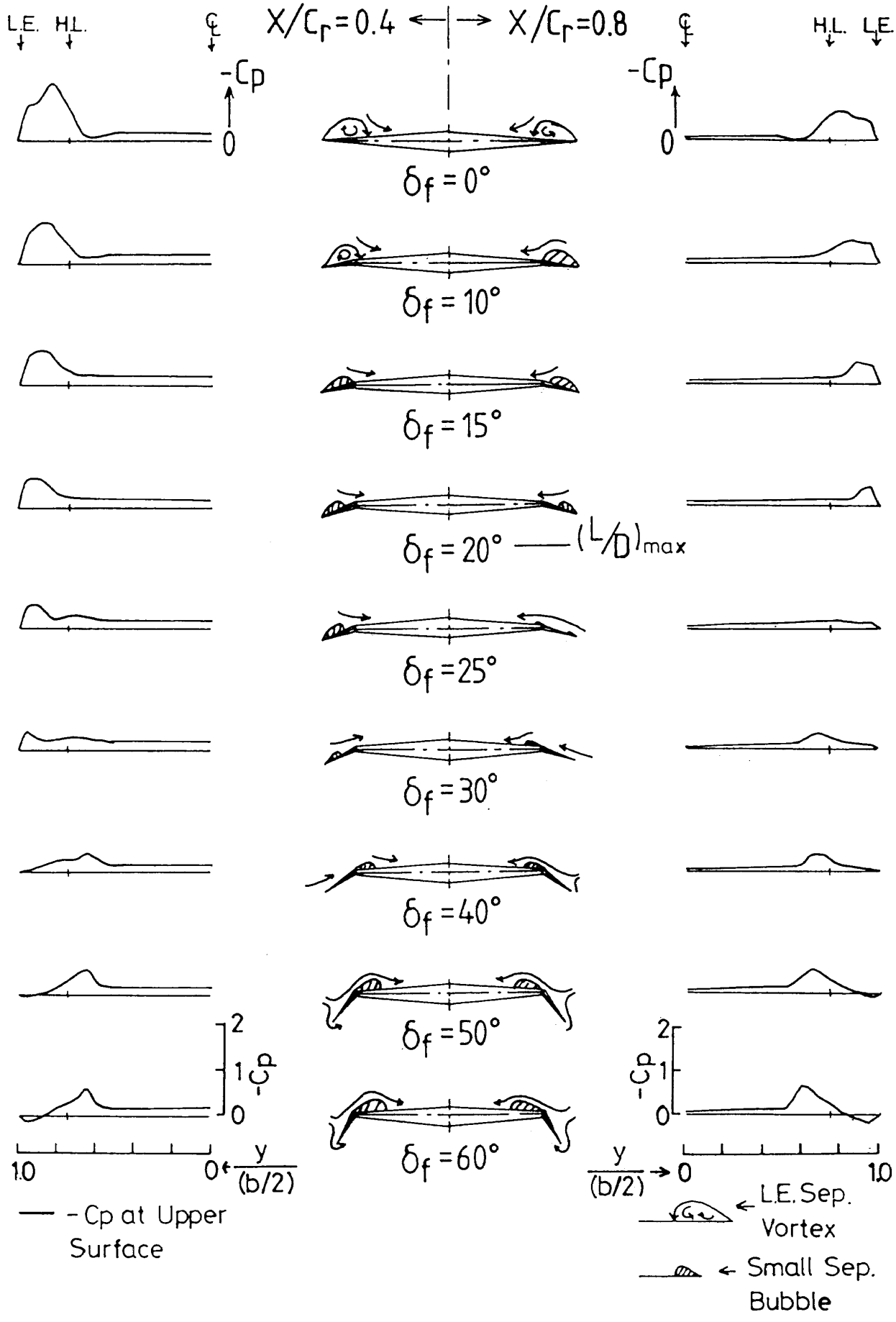

b) $\alpha_g = 8°$

Fig. 18 (Continued)

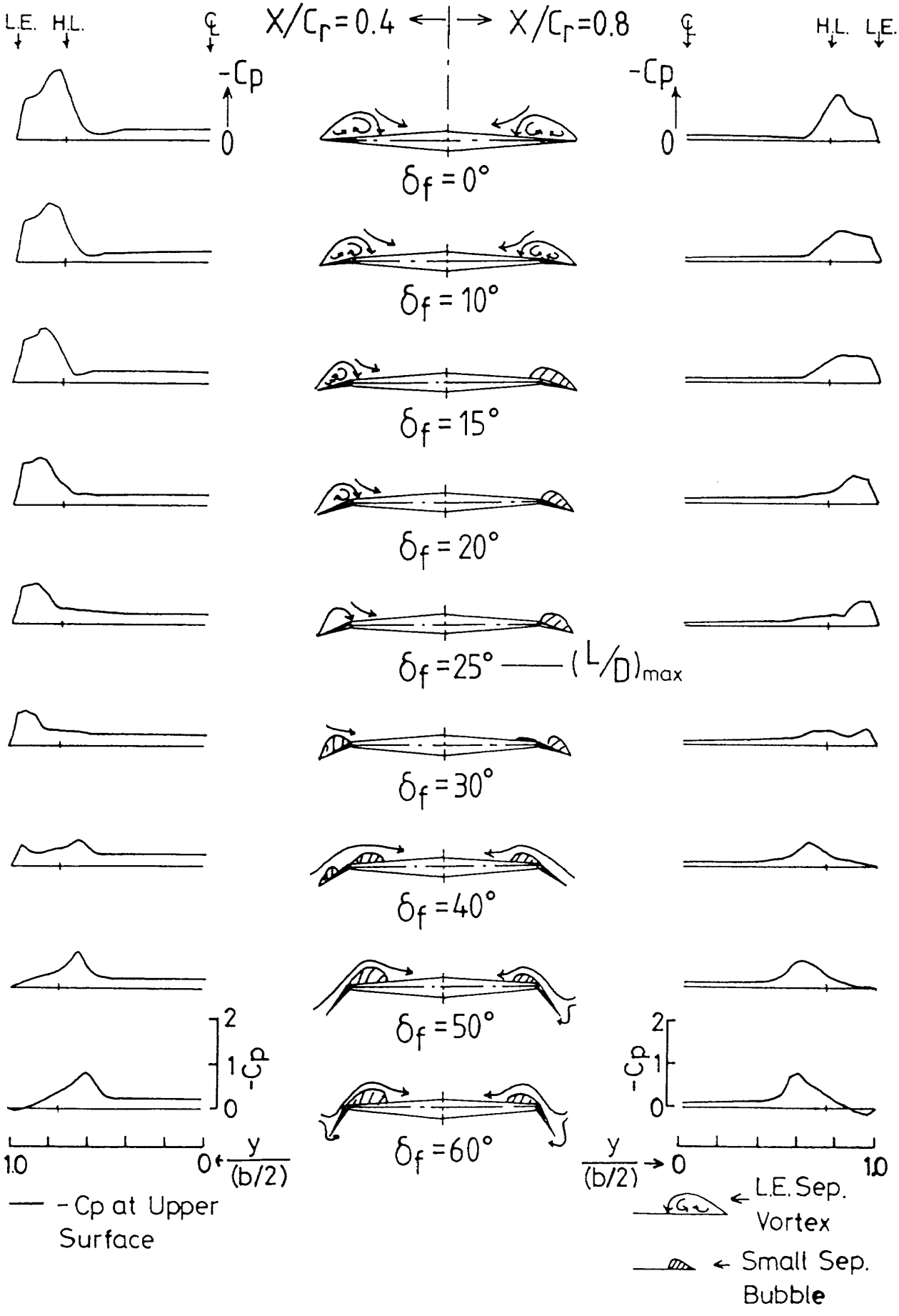

c) $\alpha_g = 10°$

Fig. 18 (Continued)

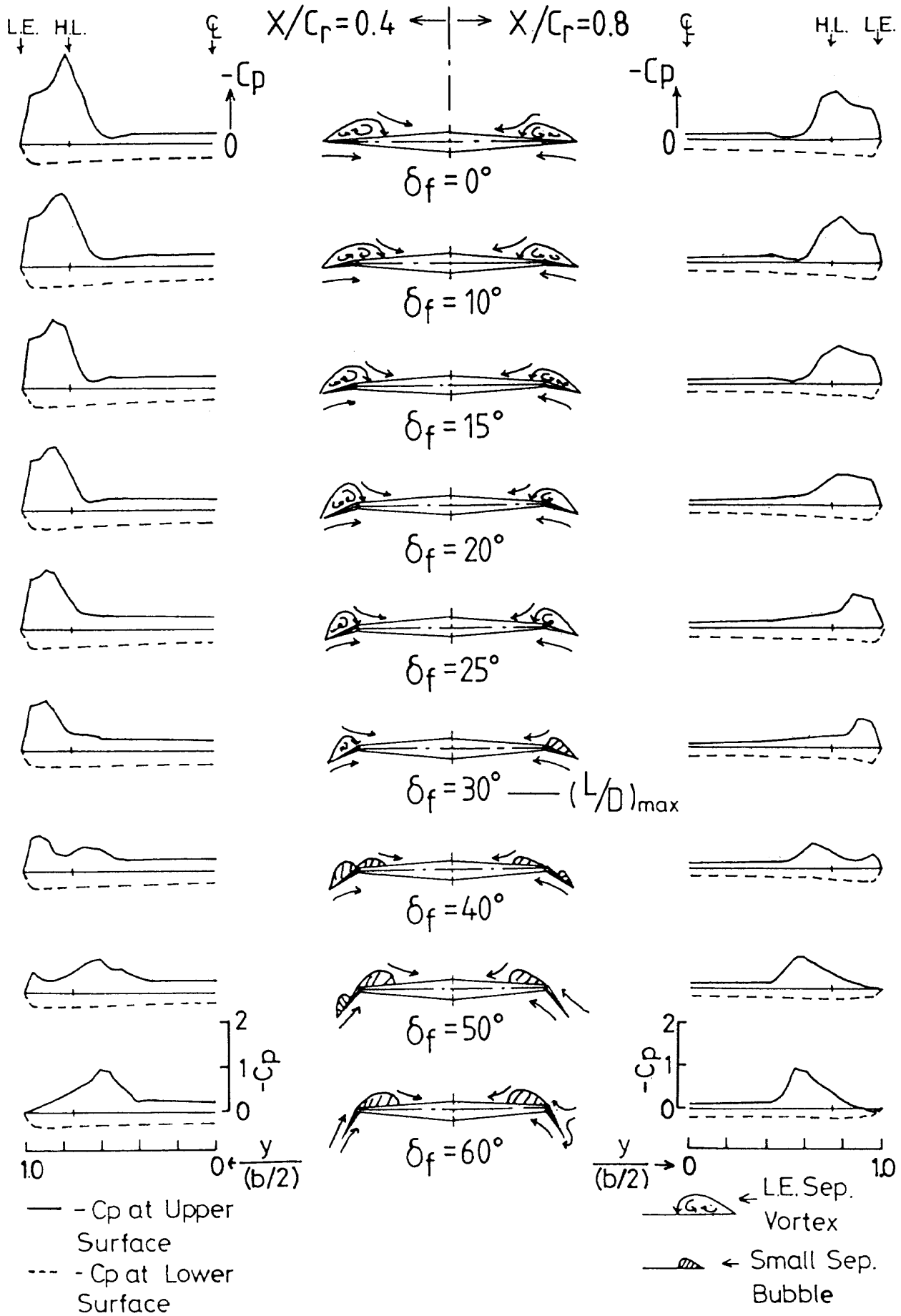

d) $\alpha_g = 12°$

Fig. 18 (Continued)

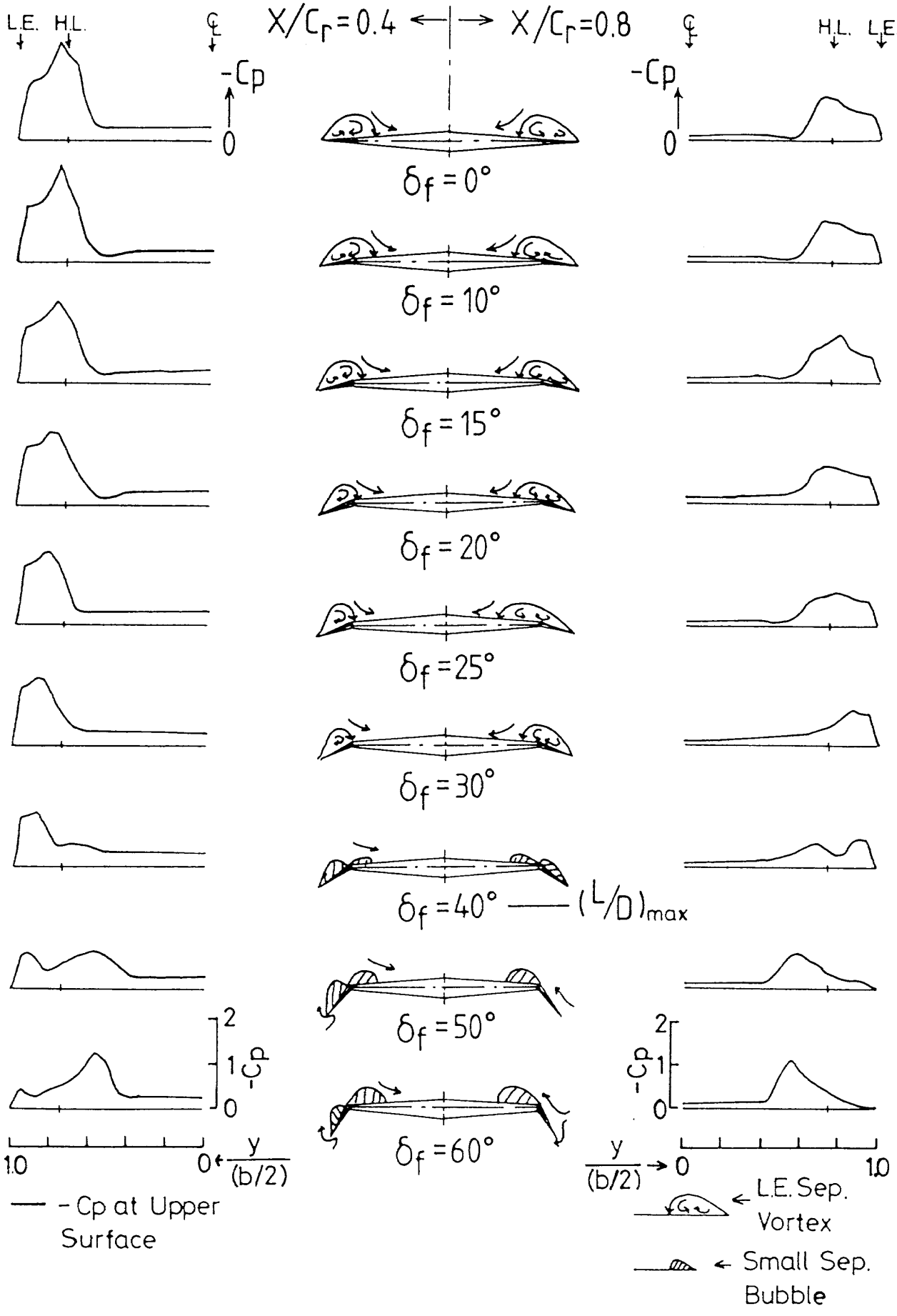

e) $\alpha_c = 14^\circ$

Fig. 18 (Continued)

as it did at the lower incidence (α_g = 6°). As δf increases above δf = 30°, the separation region is formed not only on the flap surface, but also inboard of the flap hinge line (e.g. δf = 40°). At δf = 60°, the vortex on the flap surface disappears and the only vortex formed is inboard of the flap hinge line. Fig. 18e (α_g = 14°) shows similar results to Fig. 18d.

3.2.3 C_D vs. C_L and Cross Flow Patterns

Fig. 19 shows C_D vs. C_L curves at constant incidence (α_g = 6° and 12°) together with the corresponding flow pattern sketches in the transverse plane at x/C_r = 0.4. This figure is shown in order to summarize the above results. The point where the L/D attains its maximum at each incidence is specially marked. The C_D vs. C_L curves show that the C_L increases as the δf decreases at constant incidence and that the L/D ratio attains its maximum near the point where C_D is a minimum.

At the smaller incidence (α_g = 6° the left hand curve of Fig. 19), when the flap deflection angle is zero (δf = 0° at α_g = 6°), a large leading-edge separation vortex is formed on the flap surface. Because of the suction effect of this vortex the C_D has a large value. At a flap deflection of 20°, only a small separation bubble is formed onto the flap and at δf = 25° no bubble is formed at all. Since the flow comes almost smoothly onto the flap, the C_D has a much smaller value than that at δf = 0°. Further increase of δf causes the flow to separate at the flap hinge line and a separated region is formed inboard of the hinge line (δf = 40° and 60° at α_g = 6°). Primarily because of this separated region inboard of the hinge line, the C_D of the δf = 40° and 60° configurations have greater values than those of the δf = 20° and 25° cases.

At the larger incidence of 12° (the right hand curve of Fig. 19), for both small δf (δf = 15°) and large δf (δf = 60°), the flow is similar to the patterns drawn for α_g = 6°. However, when the L/D attains its maximum value (δf = 30°), the leading-edge separation vortex is formed entirely over the flap surface and the flow reattaches near the flap hinge

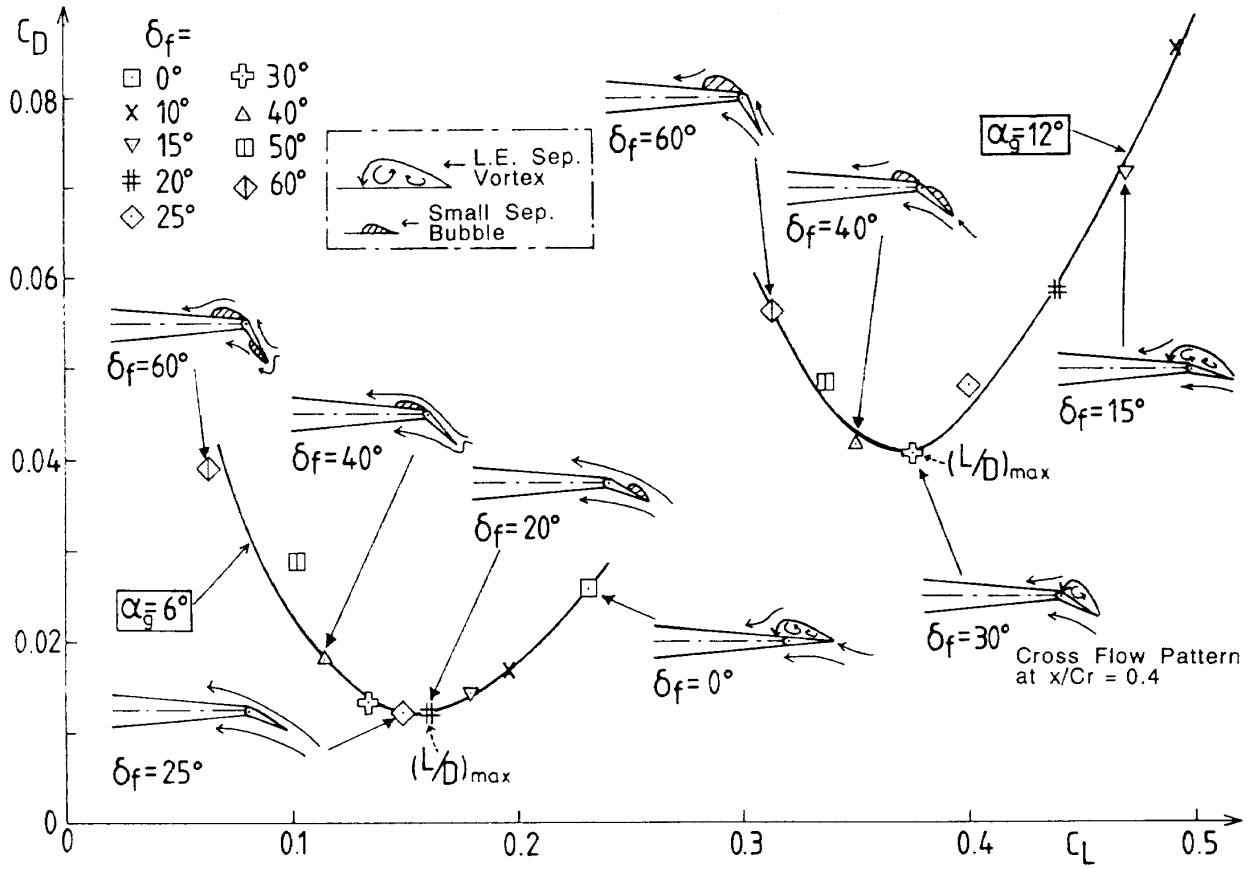

Fig. 19 C_D vs. C_L and Cross Flow Patterns at α_g = 6° & 12°

line. Because the vortex is formed only on the LEVF surface and the suction force of this vortex acts perpendicular to the deflected flap, the C_D shows a smaller value than those at other δf smaller than 30°, as was explained in Section 1. Fig. 10 showed that the maximum L/D improvement for the δf = 30° is attained between C_L values of 0.4 and 0.5. This C_L region almost coincides with that where the leading-edge vortex is formed only on the LEVF surface.

The $(L/D)_{max}$ at α_g = 6° is larger than that at α_g = 12°, as was shown in Fig. 17. This implies that the highest L/D is attained when the flow comes smoothly onto the flap surface. A similar conclusion was reached in Ref. 5 where the wing model has a different cross section (bevelled edges) to the present model. This highest L/D ratio is reached at a small value of C_L. If a larger C_L is needed from a given configuration then a larger incidence is needed and the best L/D that can be achieved appears to be with the leading-edge vortex entirely on the flap and reattachment near the hinge line.

In these tests, measurements at fixed incidences lower than 6° with varying δf were not made. Therefore, we cannot be certain that L/D attains its absolute maximum at δf = 20° and α_g = 6°. In order to confirm the highest value of $(L/D)_{max}$, it would be useful to make similar measurements at α_g = 2° and 4°.

3.3 Vortex Plate

3.3.1 Parallel Vortex Plate

Fig. 20 shows the C_L vs. α curves for two different chordwise parallel vortex plate positions together with the datum wing. This shows that the effect of the parallel vortex plate on lift is quite small. Fig. 21 shows the C_D vs. α curves. At incidences greater than 8°, the drag with the vortex plate fitted is smaller than the datum wing. This trend agrees with the results of Ref. 5. Fig. 22 shows the L/D ratio vs. C_L. For the case of g/C_r = 0, although the

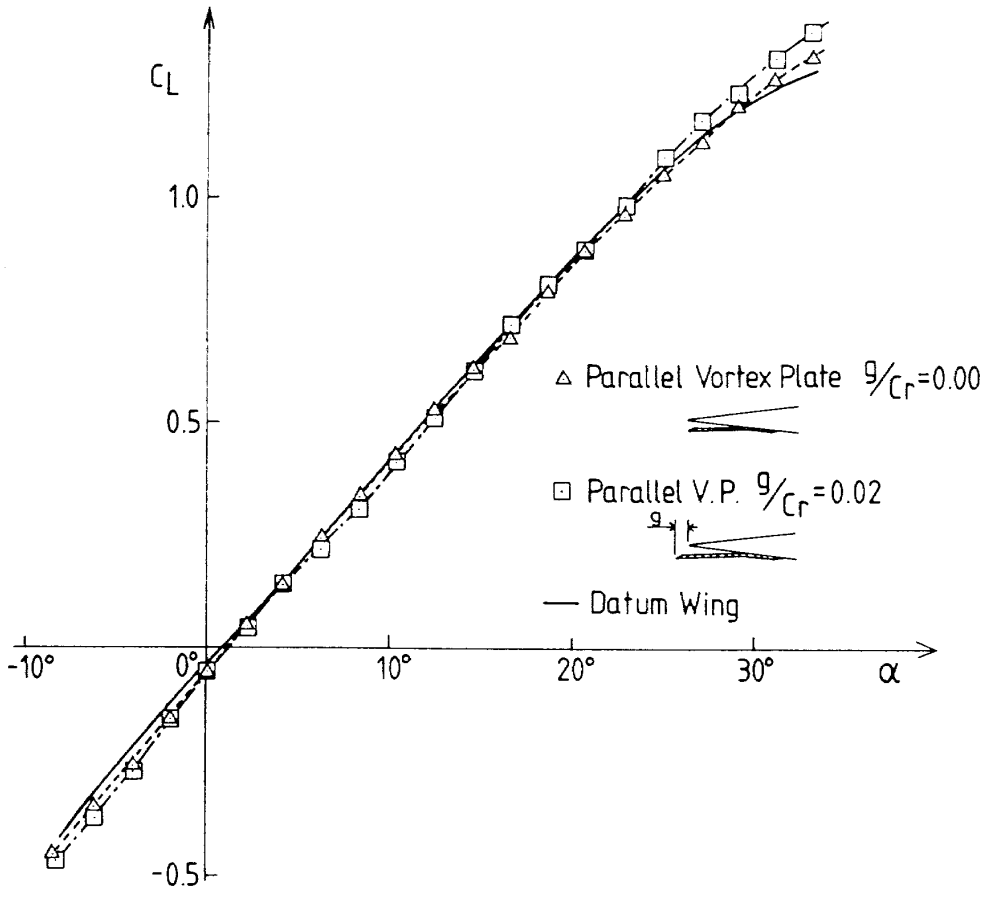

Fig. 20 Effect of Parallel Vortex Plate on C_L vs. α

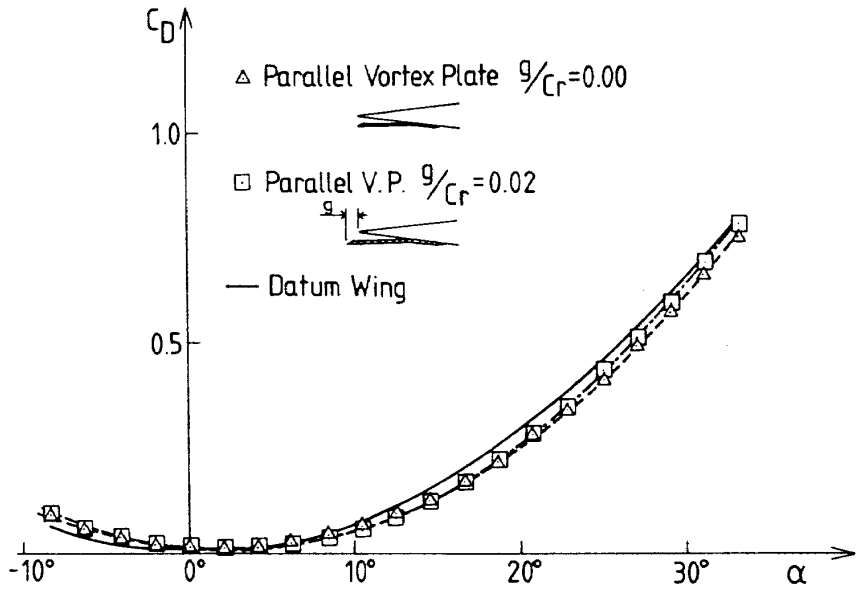

Fig. 21 Effect of Parallel Vortex Plate on C_D vs. α

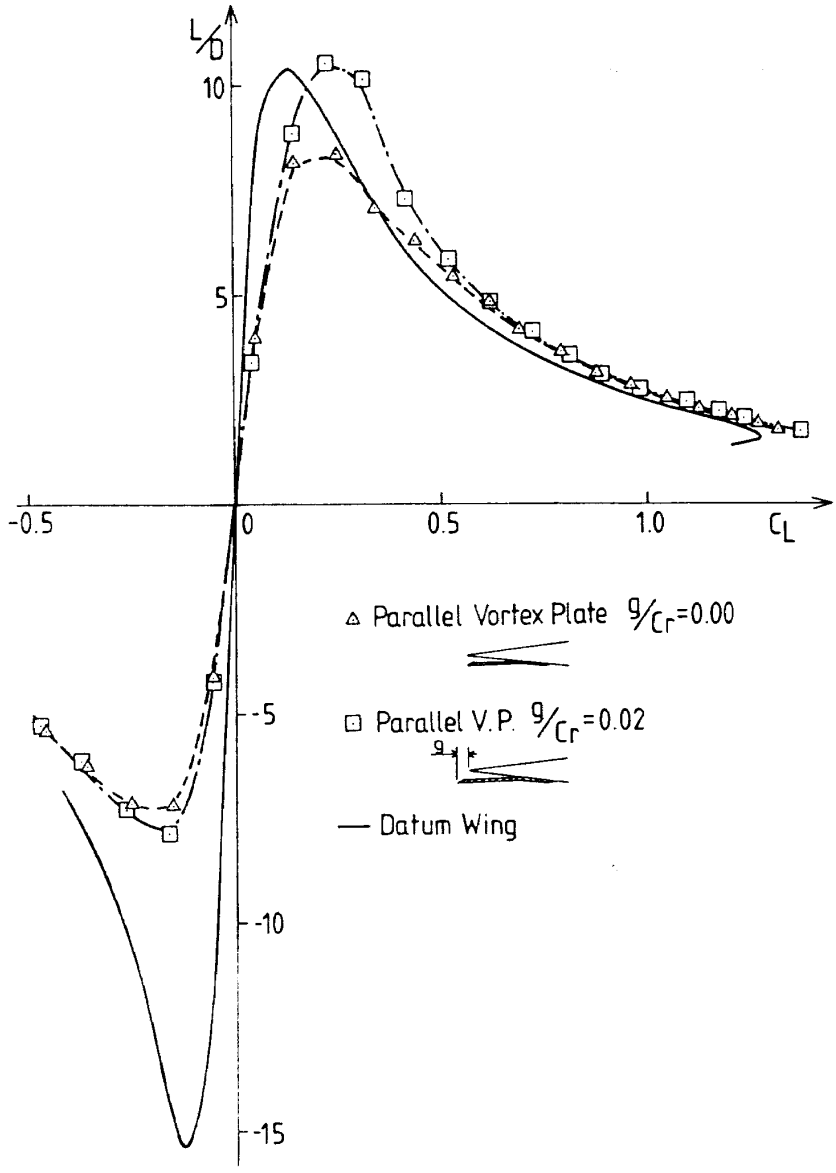

Fig. 22 Effect of Parallel Vortex Plate on L/D vs. C_L

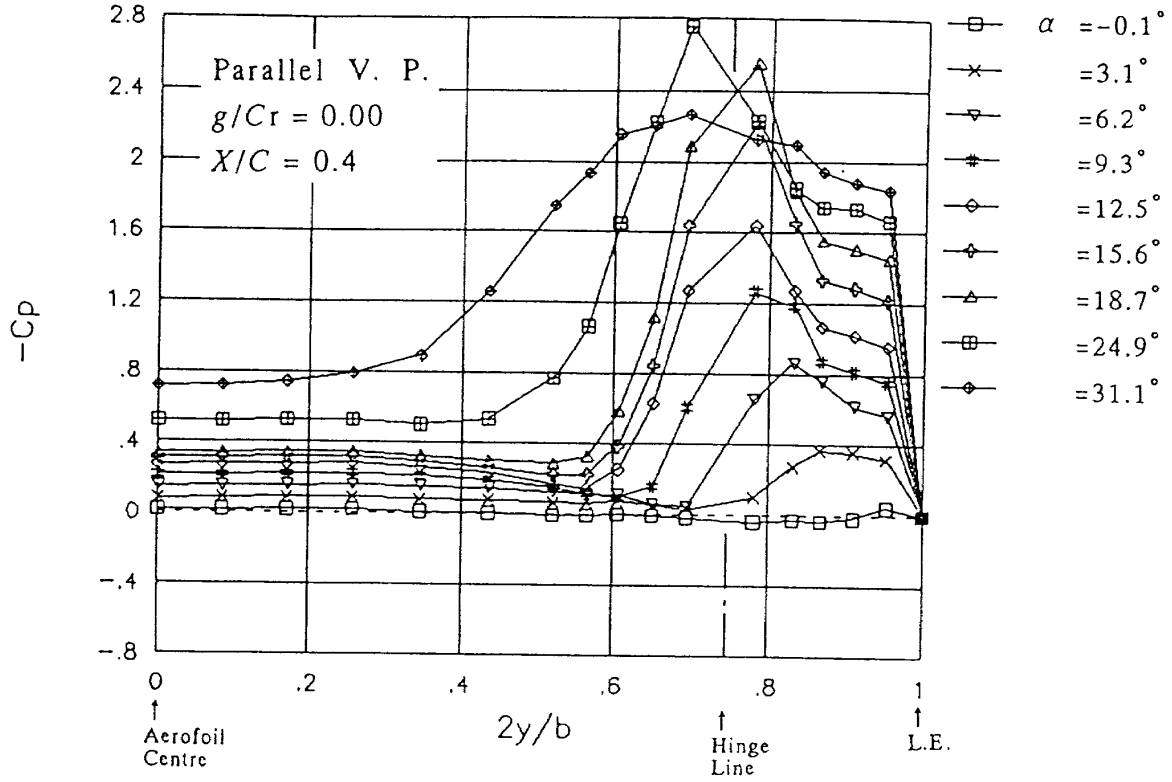

a) $g/C_r = 0.0$

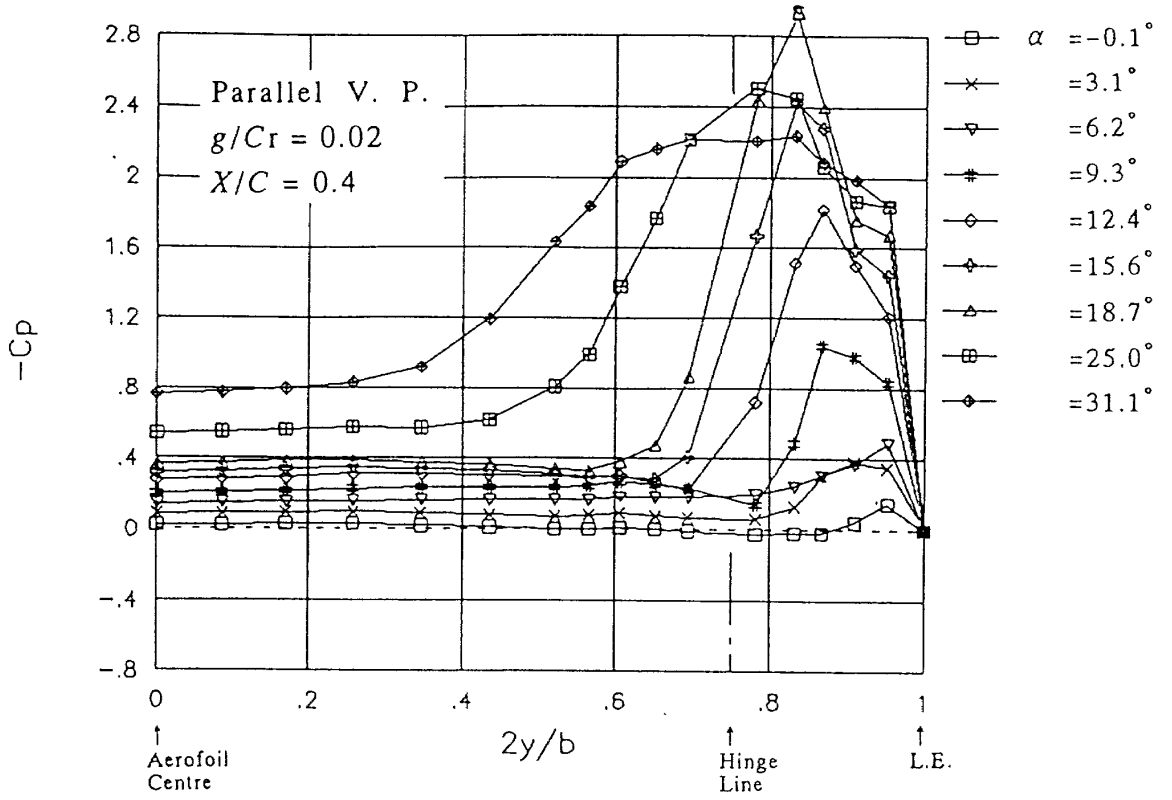

b) $g/C_r = 0.02$

Fig. 23 Surface Pressure Distributions (Parallel Vortex Plate)

maximum value of L/D is reduced in comparison with the datum wing, the L/D ratio is improved for all C_L values greater than 0.4.

For the case of $g/Cr = 0.02$ the maximum value of L/D is almost the same as that of the datum wing but it is achieved at a larger value of C_L. The L/D ratio is better with the vortex plate fitted for all values of C_L greater than 0.2. In comparison with the LEVF results, the L/D for $g/Cr = 0.02$ is roughly similar to that of the $\delta f = 30°$ at positive C_L, although the maximum value is somewhat smaller (Fig. 9). The C_m distributions of the parallel vortex plate are shown in Fig. 11 together with the other cases. The parallel vortex plate has little effect on C_m, as was found for the LEVF.

Figs. 23a ($g/Cr = 0.0$) and 23b ($g/Cr = 0.02$) show surface pressure distributions for the upper surface at $x/Cr = 0.4$. Fig. 23a shows that the C_p distributions $g/Cr = 0.0$ are quite similar to those of the datum wing (Fig. 12). This means that the parallel vortex plate ($g/Cr = 0.0$) has little effect on the flow over the upper surface. Fig. 23b shows that there is only a small separation region at $\alpha = 6.2°$ on the wing with the vortex plate ($g/Cr = 0.02$) although a leading edge separation vortex is formed on the datum wing at the same incidence as was shown in Fig. 12a. Increasing the incidence to 15.6°, there is a leading-edge separation vortex on the wing, but the spanwise length of this vortex is about 10% shorter than that on the datum wing at the same incidence. (Fig. 12a) These results suggest that onset of the leading-edge separation vortex is delayed by the vortex plate ($g/Cr = 0.02$), as was reported in Ref. 5.

3.3.2 Tapered Vortex Plate

Fig. 24 shows the C_L vs. α curves of the tapered vortex plates with and without vortex flap deflection. In this section, the results of the tapered vortex plate tests in the figures are not connected by lines in order to distinguish them from the results of the datum wing and $\delta f = 30°$ results. The C_L for the

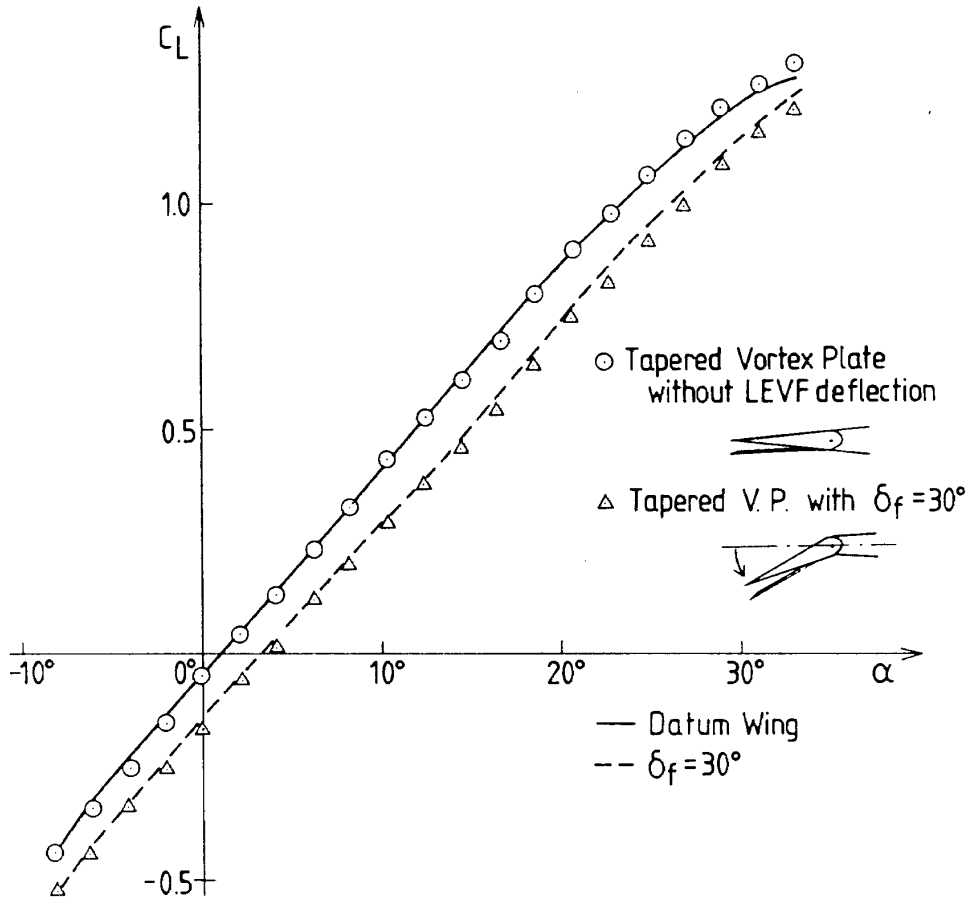

Fig. 24 Effect of Tapered Vortex Plate on C_L vs. α

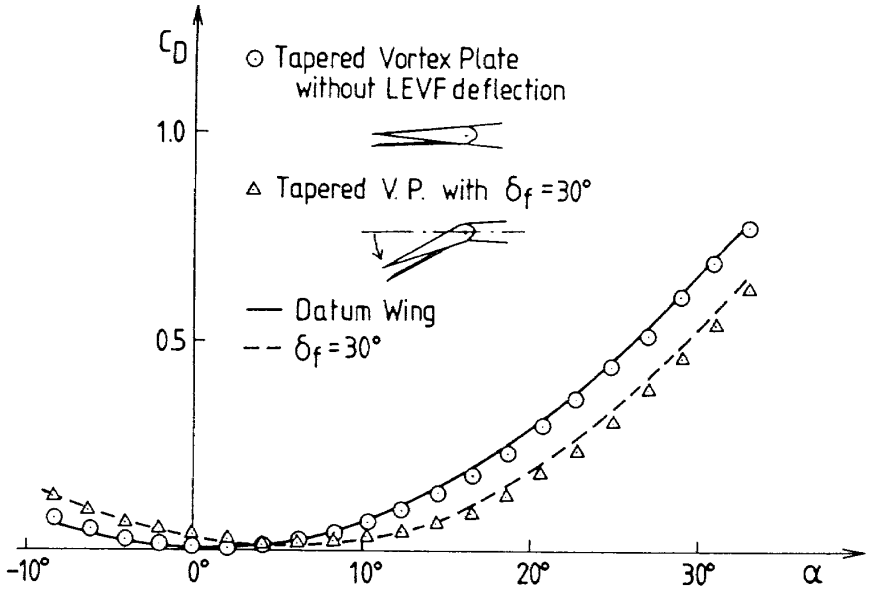

Fig. 25 Effect of Tapered Vortex Plate on C_D vs. α

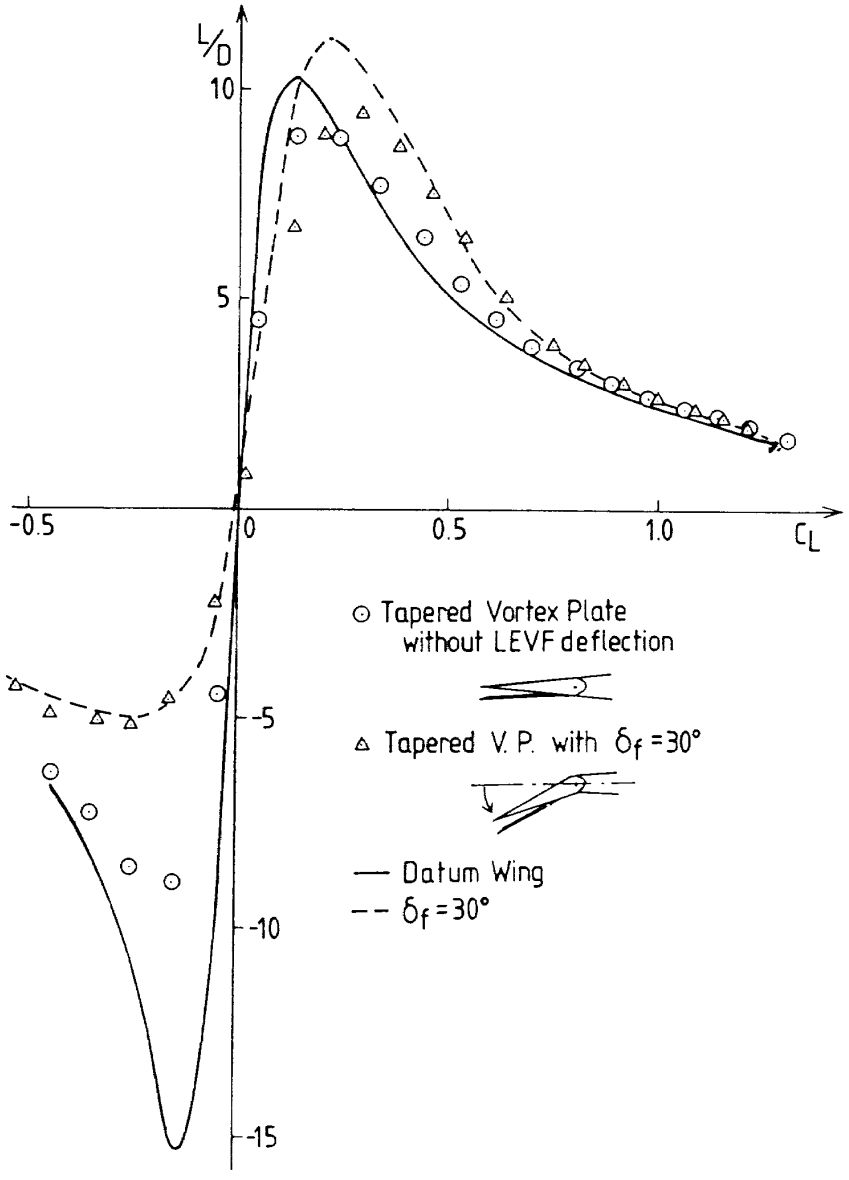

Fig. 26 Effect of Tapered Vortex Plate on L/D vs. C_L

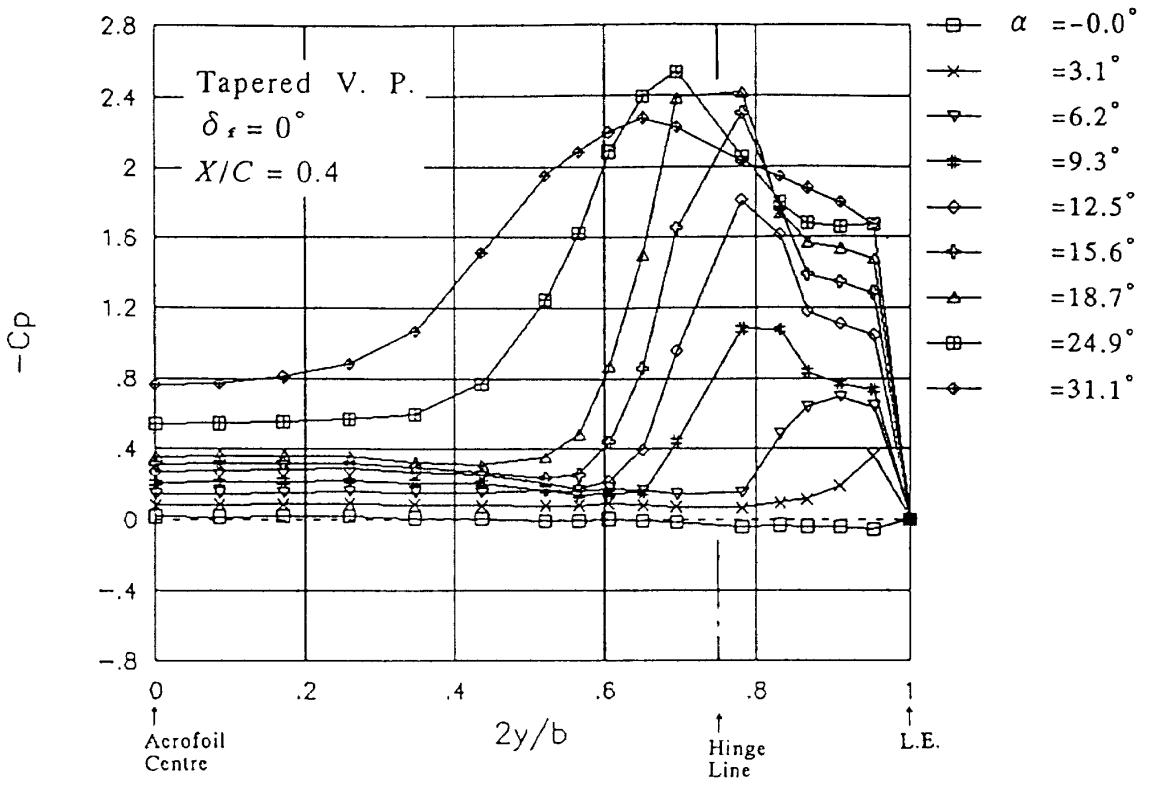

a) without LEVF Deflection

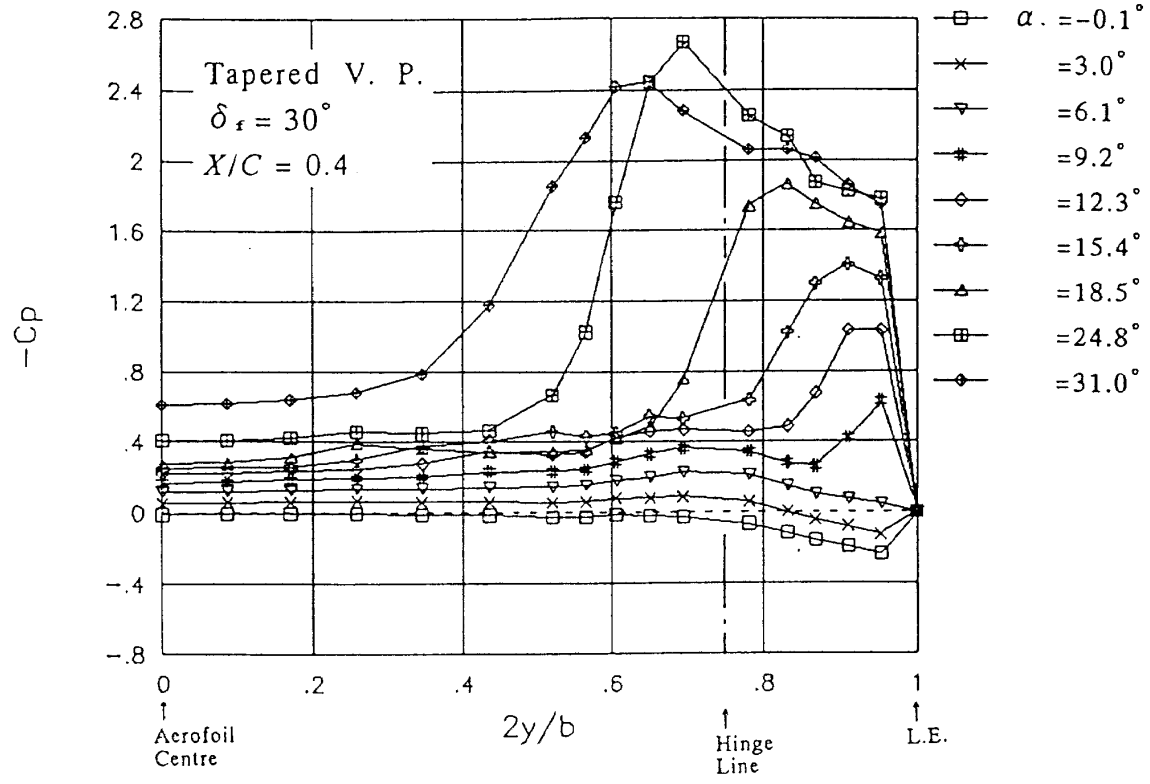

b) with $\delta_f = 30°$

Fig. 27 Surface Pressure Distributions (Tapered Vortex Plate)

tapered vortex plate without LEVF deflection is similar distribution to that of the datum wing. The C_L for the tapered vortex plate with $\delta f = 30°$ is slightly smaller than that of the LEVF alone ($\delta f = 30°$) at every incidence. Fig. 25 shows the C_D vs. α curves. The drag of the tapered vortex plate without LEVF deflection (i.e. $\delta f = 0°$) is smaller than that of the datum wing. The drags of the tapered vortex plate with $\delta f = 30°$ is smaller than that of the LEVF alone ($\delta f = 30°$). The drag reductions are most significant at the higher incidences. Fig. 26 shows the L/D ratio vs. C_L. For the tapered vortex plate without LEVF deflection (i.e. $\delta f = 0°$), the maximum value of L/D is smaller than that of the datum wing. The L/D ratio is slightly improved for C_L values greater than 0.3 when compared with results for the datum wing. This is caused by the reduction of the drag as was seen in Fig. 27. For the tapered vortex plate with $\delta f = 30°$, there is no benefit at any C_L value. The C_m vs. C_L distributions of the tapered vortex plate are shown in Fig. 11. The fitting of tapered vortex plates has very little effect.

Fig. 27a shows surface pressure distributions for the tapered vortex plate without LEVF deflection. Although suctions at incidences of 6.2° and 9.3° at $x/C_r = 0.4$ are slightly smaller than those of the datum wing at the same incidences, the C_p distributions are almost the same as those of the datum wing (Fig. 12a). Fig. 27b shows C_p distributions for the tapered vortex plate with $\delta f = 30°$. It is seen that the spanwise length of the leading-edge separation vortex at incidences 12.3°, 15.4° and 18.5° at $x/C_r = 0.4$ is shorter than that of the $\delta f = 30°$ case at the same incidences. (Fig. 13a)

4. Discussion

In this section, the leading-edge suctions recoverable through vortex flap and vortex plate deployments are discussed. The drag of a flat plate wing with no leading-edge suction is:

$$C_D = C_{D0} + C_L \tan \alpha,$$

where C_{D0} is the zero-lift drag coefficient which depends on the surface skin friction and the form drag. Using the measured C_L and C_{D0}, C_D assuming 0% leading-edge suction is calculated from the above formula and is plotted on the C_D vs. C_L curves together with the measured data in Figs. 25a–f. In order to plot the 0% leading edge suction curves, $dC_L/d\alpha$ was assumed to be equal to the measured value.

In contrast, a wing with a well rounded leading-edge can show a large drag reduction due to the leading-edge suction. In order to give some idea of the magnitude of this leading-edge suction, experimental data taken from Ref. 11 for a wing with a well rounded leading-edge are also plotted. (Figs 28a and b) In Ref. 11, measurements were made at a Reynolds number of 18.6 million (based on the root chord), using a 0.91 m span 60° delta wing which had a 10% thickness ratio aerofoil section. The nose radius was 0.69% of the chord length.

Fig. 28a shows the results for our datum wing. The measured drag polar shows almost the same value as that of the 0% leading-edge suction estimate at all incidences. This confirms that the datum wing with a sharp leading-edge develops no leading-edge suction force.

Fig. 28b shows the drag results for the wing with the LEVF deflected 30°. The measured value is considerably less than that estimated assuming zero leading-edge suction, for all incidences. When compared with the rounded leading-edge data (Ref. 11), it can be seen that the vortex flap achieves a significant amount of C_D reduction.

The results for the two parallel vortex plates (Figs. 28c and d) show that the measured drag value is less than that for the zero leading-edge suction estimate at all positive incidences. The amount of C_D reduction is almost the same for both g/C_r cases. This means that some leading-edge suction is recovered by incorporating a vortex plate. It is not clear that this C_D reduction is caused by the suction effect of a separation vortex between the leading-edge of the wing and that of the vortex plate, as was suggested in Ref. 4. Smoke visualization tests, made on a different model with vortex plates in Ref. 5, did not confirm the existence of this

vortex. It may be that the suction force is produced by the separated flow acting on the forward facing region between the wing and the vortex plate. Because of this, the C_D is reduced (as was shown in Fig. 21) and the L/D improved for C_L values greater than 0.4 (as was shown in Fig. 22).

The decrease in L/D ratio for small values of C_L (Fig. 22) is probably due to differences in the values

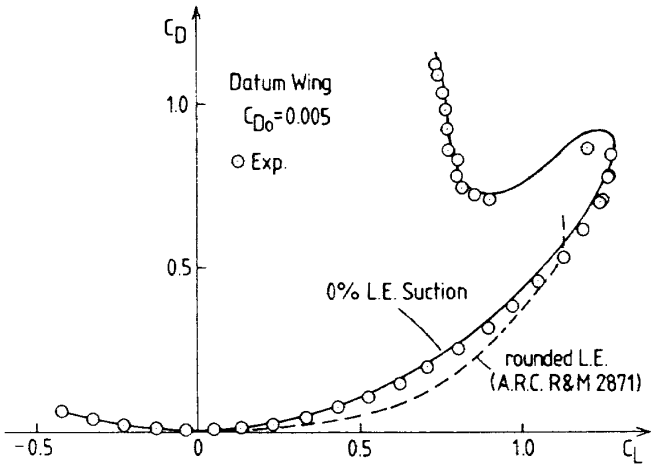

a) Datum Wing

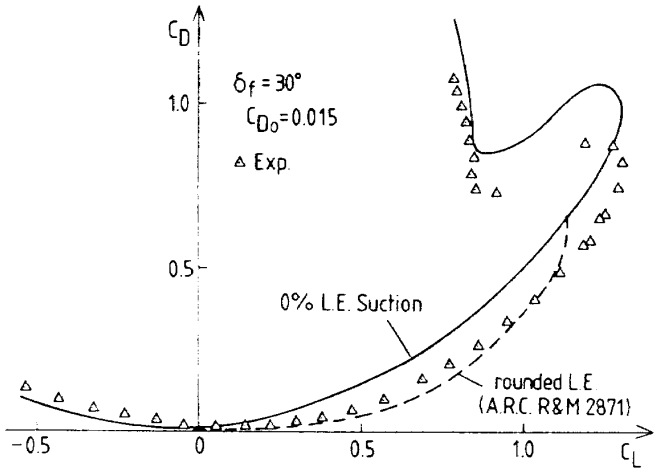

b) $\delta f = 30°$

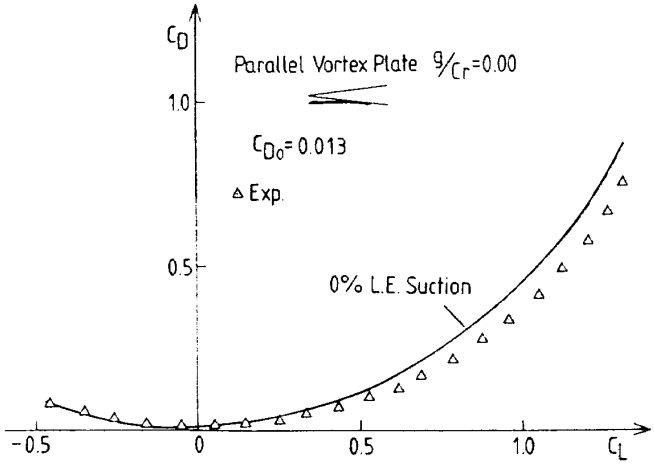

c) Parallel Vortex Plate $g/Cr = 0.00$

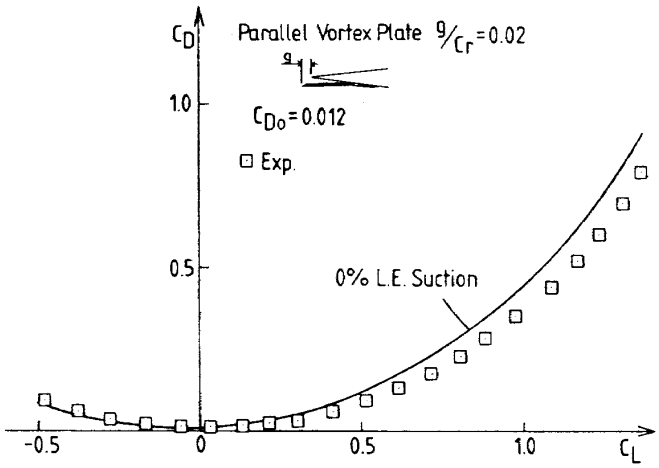

d) Parallel Vortex Plate $g/Cr = 0.02$

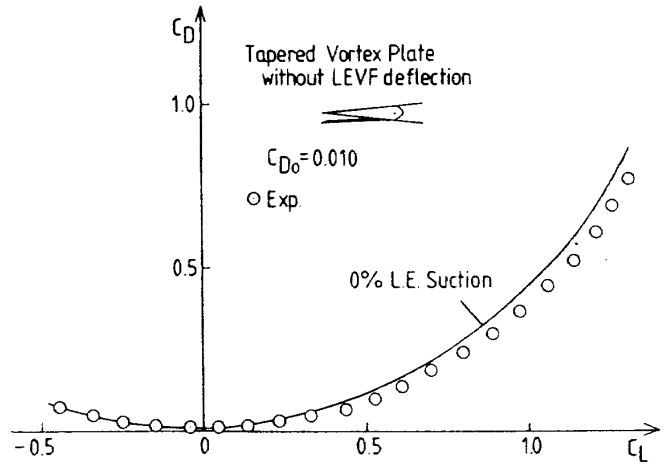

e) Tapered Vortex Plate without LEVF Deflection

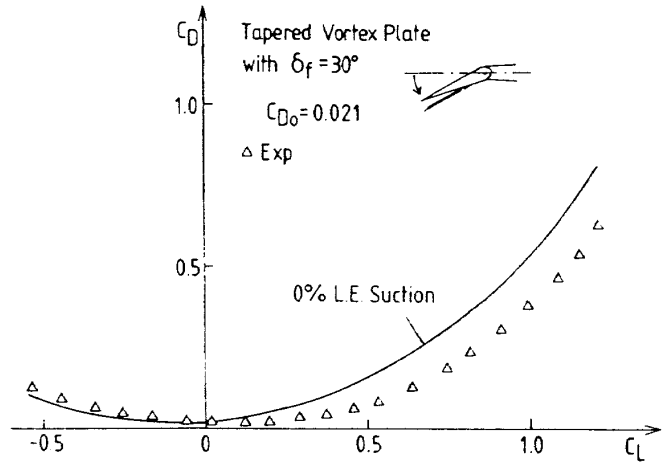

f) Tapered Vortex Plate with $\delta f = 30°$

Fig. 28 Effect of Leading-Edge Suction Force on C_D

of C_{D0}. The C_{D0} of the parallel vortex plate configuration is larger than that of the datum wing because of the difference of the forward facing area. Since a small increase in C_D causes a large decrease in L/D ratio at low values of C_L, the result is a reduction in the L/D values for the wing fitted with parallel vortex plates, as shown in Fig. 22.

Fig. 28e (the tapered vortex plate with no flap deflection) again shows the existence of a C_D reduction at all incidences. However, the C_D reduction is slightly smaller than that for the parallel vortex plate. (Fig. 28c) The vertical distance between the leading-edge of the wing and the vortex plate is 10 mm as measured at the wing tip. This is the same as for the parallel vortex plate. However, this gap decreases towards the apex as shown in Fig. 4. Therefore, the total forward facing area between the tapered vortex plate and the wing is smaller than that for the parallel plate. The leading-edge suction acting on a smaller area gives a smaller drag reduction.

When compared with the results of the tapered vortex plate with 30° LEVF deflection (Fig. 28f) and those of the LEVF alone (Fig. 28b), the C_D reduction is almost the same. Although the pressure measurements (Fig. 27b) show that the vortex formation is slightly delayed for the vortex plate with δf = 30°, the benefit of this type of vortex plate is not shown in Fig. 26. This may be explained by the fact that the forward facing area is too small as described above. Furthermore, the C_{D0} is larger than that of the LEVF (δf = 30°) alone. The results is that the maximum L/D of the tapered vortex plate with δf = 30° is smaller than that of the LEVF alone as seen in Fig. 26.

The model tested here with a tapered vortex flap had only a small forward facing area at the leading-edge. The results showed no benefit in L/D. It would be worthwhile testing another configuration with an increased gap height.

5. Conclusion

1) The improvements in lift/drag ratio obtained by deflecting a leading-edge vortex flap (as reported in Ref. 3) were confirmed.
2) There is no benefit from the vortex flap at incidences higher than the stalling incidence.
3) The highest value of $(L/D)_{max}$ is achieved using a modest flap deflection angle with the wing at, or close to, the rather small incidence for which the flow comes smoothly onto the flap.
4) At incidences higher than in 3), the L/D reaches a local maximum when the vortex flap is deflected so that a leading-edge separation vortex is formed on the LEVF top surface with the reattachment line coincident with the flap hinge line, (as was suggested in Ref. 1). However this 'local' value of $(L/D)_{max}$ is smaller than that in 3).
5) The L/D ratio of the basic wing (no LEVF) is improved by incorporating a parallel vortex plate, especially when the plate protrudes ahead of the leading-edge of the wing. The improvement measured here was comparable to that obtained from the LEVF deflection of 30°.
6) The tapered vortex flap with or without the LEVF deflected showed no significant improvement in L/D ratio.
7) There is very little change of pitching moment for any of the leading-edge devices tested here.

Acknowledgement

We would like to thank Dr. K.P. Garry, Mr. M.F. Goodridge and members of the aerodynamics department workshop in Cranfield for their help in performing the wind tunnel experiments. We also express our appreciation to Mr. P.B. Earnshaw, RAE, Farnborough, for his advice and help in carrying out this research.

References

1) Rao, D.M. Leading-Edge Vortex-Flap Experiments on a 74 deg. Delta wing, NASA CR-159161, 1979.
2) Campbell, J.F. and Osborn, R.F. Leading-Edge Vortex Research: Some Nonplanar Concepts

and Current Challenges, NASA CP-2416, pp. 31-63, 1986.

3) Stollery, J.L. and Ellis, D.G. The Behaviour and Performance of Leading-Edge Vortex Flaps, ICAS-88-4.5.2, pp. 758-765, 1988.
4) Rao, D.M. and Johnson Jr., T.D. Investigation of Delta Wing Leading-Edge Devices, J. Aircraft, Vol. 18, No. 3, pp. 1051-1056, 1981.
5) Rinoie, K. Experimental Studies of Vortex Flaps and Vortex Plates Part 1. 0.53 m Span 60° Delta wing, NAL TR-1140T, March 1992.
6) Rae Jr., W.H. and Pope, A. Low-Speed Wind Tunnel Testing (2nd Ed.), JOHN WILEY & SONS, New York, 1984.
7) Pankhurst, R.C. and Holder, D.W. Wind-Tunnel Technique; an Account of Experimental Methods in Low- and High-Speed Wind Tunnels, PITMAN, London, 1952.
8) Küchemann, D. The Aerodynamic Design of Aircraft, PERGAMON PRESS, Oxford, 1978.
9) Earnshaw, P.B. and Lawford, J.A. Low-Speed Wind-Tunnel Experiments on a Series of Sharp-Edged Delta Wings, A.R.C. Tech. Report R. & M. No. 3424, 1964.
10) Jaquet, B.M. and Brewer, J.D. Low-Speed Static-Stability and Rolling Characteristics of Low-Aspect-Ratio Wings of Triangular and Modified Triangular Plan Forms, NACA RM No. L8L29, 1949.
11) Jones, R., Miles, C.J.W. and Pusey, P.S. Experiments in the Compressed Air Tunnel on Swept-back wings including two delta wings, A.R.C. Tech. Report R. & M. No. 2871, 1954.

TECHNICAL REPORT OF NATIONAL
AEROSPACE LABORATORY
TR-1180T

航空宇宙技術研究所報告1180T号(欧文)

平成4年10月発行

発行所 航空宇宙技術研究所
東京都調布市深大寺東町7丁目44番地1
電話三鷹(0422)47-5911(大代表)〒182
印刷所 株式会社 東京プレス
東京都板橋区桜川2－27－12

Published by
NATIONAL AEROSPACE LABORATORY
7-44-1 Jindaijihigashi-Machi Chōfu, Tokyo
JAPAN

Printed in Japan